Differentiating Hund from Mott physics in a three-band Hubbard-Hund model: Temperature dependence of spectral, transport, and thermodynamic properties

K. M. Stadler,[1] G. Kotliar,[2,*] S.-S. B. Lee,[1] A. Weichselbaum,[3,1] and J. von Delft[1,†]

[1] *Arnold Sommerfeld Center for Theoretical Physics, Center for NanoScience, and Munich Center for Quantum Science and Technology, Ludwig-Maximilians-Universität München, 80333 Munich, Germany*
[2] *Department of Physics and Astronomy, Rutgers University, Piscataway, NJ 08854, USA*
[3] *Condensed Matter Physics and Materials Science Department, Brookhaven National Laboratory, Upton, New York 11973, USA*

We study the interplay between Mott physics, driven by Coulomb repulsion U, and Hund physics, driven by Hund's coupling J, for a minimal model for Hund metals, the orbital-symmetric three-band Hubbard-Hund model (3HHM) for a lattice filling of 1/3. Hund-correlated metals are characterized by spin-orbital separation (SOS), a Hund's-rule-induced two-stage Kondo-type screening process, in which spin screening occurs at much lower energy scales than orbital screening. By contrast, in Mott-correlated metals, lying close to the phase boundary of a metal-insulator transition, the SOS window becomes negligibly small and the Hubbard bands are well separated. Using dynamical mean-field theory and the numerical renormalization group as real-frequency impurity solver, we identify numerous fingerprints distinguishing Hundness from Mottness in the temperature dependence of various physical quantities. These include ARPES-type spectra, the local self-energy, static local orbital and spin susceptibilities, resistivity, thermopower, and lattice and impurity entropies. Our detailed description of the behavior of these quantities within the context of a simple model Hamiltonian will be helpful for distinguishing Hundness from Mottness in experimental and theoretical studies of real materials.

I. INTRODUCTION

The properties of multiorbital metals with strong onsite atomic-like interactions is governed by strong correlation effects. In this paper, we study the interplay of two distinct manifestations of local interactions: "Mott physics", driven by the Coulomb repulsion U governing charge dynamics; and "Hund physics", driven by the Hund's rule coupling J affecting spin dynamics.

For many years, strong electronic correlations in metals have mainly been associated with Mottness, well-known from ordinary Mott-Hubbard systems – in the proximity of a Mott-insulating state, U is large (compared to J) and slows down or even suppresses the electronic motion. This leads to characteristic spectral signatures like well-separated Hubbard sidebands and fairly flat bands at the Fermi level at low energies and temperatures, reflecting strongly renormalized heavy Landau quasiparticles (QPs). At high energies, typically, the quasiparticle band vanishes and a gap or pseudogap opens between the Hubbard sidebands. A well-known example is V_2O_3 [1–7].

Starting around 2008, it has been recognized that noticeable correlation effects are manifest in many multiorbital systems far from a Mott insulating state as they have occupancies differing from half integer filling [7–53]. In these systems the effect of U is considered to be too small to correlate the electrons, while Hund's coupling J is only slightly smaller in the solid than for a bare atom [54]. These so-called Hund metals are multiorbital systems with rather broad bands and thus sizeable J compared to a strongly screened U. By now the 3d iron-based superconductors [9–19] and the 4d-based ruthenates [8, 22–29] have been studied from this perspective. Other examples where Hund-rule physics is important are iron impurities on a platinum surface [55], weak itinerant ferromagnets [56], e_g systems such as $NiS_{2-x}Se_x$ [57], the recently discovered Ni-based superconductors [43, 44], and even cold atom systems [58]. For some early reviews, see Refs. [30–32].

Hund metals have many unusual characteristics, including the following: (i) Atomic histograms showing the probability weight for different electronic configurations are broad. A range of configurations featuring different orbital occupancies all receive significant weight (implying metallic behavior), and high-spin multiplets are favored (thus allowing for a quasi-localized spin) [9, 20, 59]. (ii) The orbitals appear to decouple from each other [11, 59–62] if one focuses on static correlators [36]. (iii) Spin dynamics appears to slow down at low energies ("spin freezing") [8]. (iv) Various correlators show fractional power law behavior [8, 21, 39]. (v) Correlations depend strongly on the value of J and relatively less strongly on the value of U. (vii) The interplay of spin and orbital degrees of freedom leads to "spin-orbital separation" (SOS) [7, 21, 33–39]. Here, we focus particularly on the latter phenomenon.

In an isolated atom, it is well known that J simply aligns electronic spins in different orbitals according to Hund's first rule [63]. But if the atom is hybridized with a metallic environment, as in many multiorbital materials or impurity models, the effect of J is much more intricate and subtle (and was, with a few exceptions [64], largely overlooked or underestimated until this decade). Here,

* kotliar@physics.rutgers.edu
† Correspondence: vondelft@lmu.de

SOS emerges in a complex two-stage Kondo-type screening process, in which spin screening occurs at much lower energies than orbital screening [33, 35]: $T_{\rm spin} < T_{\rm orb}$ (cf. Appendix A for precise definitions of these scales). The low-energy regime below $T_{\rm spin}$ is a Fermi liquid (FL) governed by Landau QPs with heavy masses. By contrast, the intermediate energy window featuring SOS, $[T_{\rm spin}, T_{\rm orb}]$, is governed by almost fully screened orbital degrees of freedom weakly coupled to almost free spin degrees of freedom, leading to incoherent behavior. Its non-Fermi-liquid (NFL) properties are caused by an underlying novel NFL fixed point, described in detail in Refs. [37, 39] for a 3-channel spin-orbital Kondo (3soK) model for Hund metals, as suggested in Ref. [34].

As a function of increasing temperature, SOS leads to a coherence-incoherence crossover with a coherence scale that is strongly suppressed by Hund's coupling [33]. The coherence-incoherence crossover was predicted in material simulations of iron oxypnictides already in 2008 [9, 65]. It was observed a few years later in measurements of the resistivity, heat-capacity, thermal-expansion coefficients, susceptibility, and optical conductivity of the 122-iron pnictides [66–68]. Further, only recently [7], realistic material simulations and model Hamiltonian studies of the temperature dependence of the local spectrum and of the charge, spin, and orbital susceptibilities of the Hund metal Sr_2RuO_4 and the Mott material V_2O_3 revealed that, for Hund metals, SOS also occurs in the onset (and completion) of screening of the orbital and spin degrees of freedom: as the temperature is lowered in Hund metals, the static local orbital and spin susceptibilities show deviations from Curie behavior at different scales: $T_{\rm spin}^{\rm onset} < T_{\rm orb}^{\rm onset}$. By contrast, for Mott materials we have $T_{\rm orb}^{\rm onset} \approx T_{\rm spin}^{\rm onset}$, since both these scales are equal to the scale $T_{\rm M}$ at which the Mott gap closes when the temperature is lowered.

During the last years, many insights on SOS have been gained in the context of a minimal 3-orbital Hubbard-Hund model (3HHM) for Hund metals. In Refs. [33, 35, 39] the focus has mainly been on zero-temperature results, while some finite-temperature results were published in Ref. [7]. In the present paper, we build on and extend the latter study by providing a full analysis of the *temperature dependence* of ARPES spectra, spectral function, self-energy, static local spin and orbital susceptibilities, the QP weight, scattering rate, resistivity, thermopower, and entropy. We choose four different sets of system parameters, which mimic the physics of a Hund system (H1), a Mott system (M1), an intermediate system (I2) showing aspect of both Hund and Mott physics, and a weakly correlated system (W0). With this we aim to clarify previously-proposed criteria and also identify new ones for distinguishing the two distinct routes of screening from atomic degrees of freedom towards emerging quasiparticles, guided by either Mott or Hund physics.

This paper is structured as follows. First we introduce the 3HHM in Sec. II. In Sec. III we shortly review the current state of research on the 3HHM and motivate our choice of model parameters. Sections IV, V, and VI present our results. Section IV concentrates on ARPES spectra, as well as spectral functions and self-energies. In particular, we discuss the different temperature dependencies of these quantities for Hund and Mott systems. Based on our discussion of the ARPES spectra, in Sec. V, we explain in detail the behavior of the static local orbital and spin susceptibilities and the quasiparticle weight in terms of the SOS screening process. In Sec. VI we analyze signatures of Hund and Mott systems in various transport properties (scattering rate, coherence scale, resistivity, effective chemical potential, thermopower). Further, we study the lattice entropy and demonstrate that it differs from the impurity entropy. Remarkably, we are able to calculate the lattice entropy directly from our numerical data. We summarize our insights in Sec. VII by providing tables, which highlight the most important features for distinguishing Mott and Hund physics. Appendix A additionally offers a detailed analysis of the particle-hole asymmetry of the 3HHM at $T = 0$ and of the frequency and temperature dependence of the optical conductivity. Further, it contains elementary definitions of several quantities discussed in Sec. VI.

II. MODEL AND METHOD

The minimal 3HHM model for Hund metals, first suggested in Ref. [21], is described by the Hamiltonian

$$\hat{H} = \sum_i \left(-\mu \hat{N}_i + \hat{H}_{\rm int}[\hat{d}^\dagger_{i\nu}] \right) + \sum_{\langle ij \rangle \nu} t\, \hat{d}^\dagger_{i\nu} \hat{d}_{j\nu}, \qquad (1)$$

$$\hat{H}_{\rm int}[\hat{d}^\dagger_{i\nu}] = \tfrac{1}{2}\left(U - \tfrac{3}{2}J\right) \hat{N}_i(\hat{N}_i - 1) - J\hat{\mathbf{S}}_i^2 + \tfrac{3}{4}J\hat{N}_i.$$

The on-site interaction term incorporates Mott and Hund physics through U and J, respectively. $\hat{d}^\dagger_{i\nu}$ creates an electron on site i of flavor $\nu = (m\sigma)$, composed of a spin ($\sigma = \uparrow, \downarrow$) and orbital ($m = 1, 2, 3$) index. $\hat{n}_{i\nu} = \hat{d}^\dagger_{i\nu}\hat{d}_{i\nu}$ counts the electrons of flavor ν on site i. $\hat{N}_i = \sum_\nu \hat{n}_{i\nu}$ is the total number operator for site i and $\hat{\mathbf{S}}_i$ its total spin, with components $\hat{S}_i^\alpha = \sum_{m\sigma\sigma'} \hat{d}^\dagger_{im\sigma} \frac{1}{2}\sigma^\alpha_{\sigma\sigma'} \hat{d}_{im\sigma'}$, where σ^α are Pauli matrices. We take a uniform hopping amplitude, $t = 1$, serving as energy unit in the 3HHM, and a Bethe lattice in the limit of large lattice coordination. The total width of each of the degenerate bands is $W = 4$. We choose the chemical potential μ such that the total filling per lattice site is $n_d \equiv \langle N_i \rangle = 2$, i.e., the three degenerate bands host two electrons. The effective bare gap of this model is given by $\Delta_b \equiv U - 2J$. (For a motivation of this definition, see Ref. [35].) We emphasize that Hund's coupling plays no role at filling $n_d = 1$, unless the Hund's coupling itself becomes so large that it starts mixing orbitals with different occupation. In the latter case, similar Hund's signatures may be observed even for a 2-orbital model with possible relevance to certain materials [69].

We have solved the 3HHM of Eq. (1) using dynamical mean-field theory (DMFT) [4] combined with a state-of-the-art multiband impurity solver, the full-density-matrix numerical renormalization group (fdmNRG) [70, 71], while fully exploiting the model's $\mathrm{U(1)_{ch}}\times\mathrm{SU(2)_{spin}}\times\mathrm{SU(3)_{orb}}$ symmetry using the QSpace tensor library [72]. This approach has yielded valuable insights into the complex interplay of spin and orbital degrees of freedom before [7, 33, 35, 39], because it delivers high-quality results directly on the real-frequency axes and for all physically relevant energies and temperatures. Details of the DMFT+fdmNRG method are described in Refs. [33, 35, 73]. Method-related parameters are given in the Supplementary Material of Ref. [33].

III. BACKGROUND AND SETUP

This paper is strongly based on the insights gained in Ref. [35] for the 3HHM at $T = 0$. In the following, we give a short overview of the most important facts established there. These will be used later to analyze the temperature dependence of various physical quantities in the 3HHM.

Phase diagram. In Ref. [35] we explored the 3HHM at 1/3 filling in a broad region of parameters at $T = 0$ and established the J-U phase diagram, replotted in Fig. 1(a). It consists of three different phases: a metallic phase (squares), a coexistence region (circles), and an insulating phase (triangles), separated by two phase transition lines U_{c1} (solid red curve) and U_{c2} (dashed black curve), respectively. Thus, for fixed J, a Mott insulator transition (MIT) occurs with increasing U, discussed extensively in Ref. [35]. The red color intensity of the symbols reflects the strength of the quasiparticle weight, obtained from the self-energy of the self-consistent lattice Green's function via

$$Z = \frac{1}{1 - \partial_\omega \mathrm{Re}\,\Sigma(\omega)|_{\omega=0}} = \frac{m}{m^*}, \tag{2}$$

with m the free electron mass and m^* the renormalized QP mass. Importantly, for sizeable $J \gtrsim 1$ (cf. Ref. [35] for details), strong correlation effects, i.e., considerable mass enhancements Z^{-1} occur not only close to the MIT lines but also far from it (cf. e.g., faded red color for H1).

In Ref. [35] we aimed to identify the origin of strong correlations far from and close to the MIT in Fig. 1(a). To this end, we proposed several characteristic signatures distinguishing Hund-correlated from Mott-correlated systems at $T = 0$. We briefly recapitulate the findings from Ref. [35] in the following three paragraphs.

Hund system. The 3HHM shows behavior typical of Hund metals at moderate and small U values, i.e., far from a MIT phase boundary. As a prototypical example, we choose the Hund system H1 [marked by a cross in Fig. 1(a)] with $J = 1$ and a small bare gap $\Delta_b = 1$. This choice relies on the fact that H1 qualitatively reproduces various physical properties of the Hund metal Sr_2RuO_4 [7]. At $T = 0$, Hund systems are characterized by the following signatures.

The lowest bare atomic excitation scale $E_{\mathrm{atomic}} = \omega_{e1} = -\omega_h = \frac{1}{2}U - J$ is typically small due to the small value of U and the sizable value of J (e.g., $E^{\mathrm{H1}}_{\mathrm{atomic}} = 0.5$ for H1). The bare atomic scales, ω_h, ω_{e1}, and $\omega_{e2} = \frac{1}{2}U + 2J$ define the characteristic energy scales, i.e., the peak positions, of the Hubbard bands in the local density of states,

$$A(\omega) = -\tfrac{1}{\pi}\mathrm{Im}\,[G_{\mathrm{imp}}(\omega)], \tag{3}$$

cf. yellow crosses in Fig. 1(b). Thus, for H1, the Hubbard bands form a broad incoherent background.

In Hund systems, strong correlations are induced by "Hund physics": The spin Kondo scale is strongly reduced due to SOS, with $T_{\mathrm{spin}} = 0.12$ for H1 [cf. brown curves in Fig. 1(c)]. Accordingly, the QP mass, $Z^{-1} = 3.45 \propto {T_{\mathrm{spin}}}^{-1}$ [35], is strongly enhanced. By contrast, $T_{\mathrm{orb}} = 1.20$ is even larger than $E_{\mathrm{atomic}} = 0.5$ for H1. This leads to a very broad SOS frequency window $[T_{\mathrm{spin}}, T_{\mathrm{orb}}] = 1.08$ comparable in magnitude to $\Delta_b = 1$ in Hund systems [cf. yellow vertical bar in Fig. 1(c) for H1]. The incoherent regime is strongly particle-hole asymmetric in frequency space [33, 35] and shows fractional power-law behavior [39, 73–75]. At zero temperature, the two-step SOS Kondo screening process is reflected in $A(\omega)$ in form of a two-tier QP peak on top of the broad incoherent background. It consists of a thin spin Kondo peak related to spin screening and a broader orbital Kondo peak related to orbital screening [cf. yellow curve in Fig. 1(b)] [35].

Mott system. A Mott system is by definition close to the MIT phase boundary. U is large compared to J. We choose the Mott system M1 [marked by an asterisk in Fig. 1(a)] with $J = 1$ and a large bare gap $\Delta_b \equiv U - 2J = 4.5$ as a prototypical example. M1 qualitatively reproduces various physical properties of the well-studied Mott system V_2O_3 [7]. The lowest bare atomic excitation scales $\pm E^{\mathrm{M1}}_{\mathrm{atomic}} = \pm 2.25$ are large due to the large value of U, and the Hubbard bands therefore well separated [cf. black curve in Fig. 1(b)]. By contrast, with increasing U, both T_{orb} and T_{spin} are linearly reduced, while their ratio remains constant [cf. brown curves in Fig. 1(c)]. As a consequence the SOS window is strongly downscaled $[T_{\mathrm{spin}} = 0.04, T_{\mathrm{orb}} = 0.39]$, becoming almost negligibly small compared to $\Delta_b = 4.5$ [cf. black vertical bar in Fig. 1(c) for M1]. Since both Kondo scales are small, the QP peak is narrow altogether and well separated from the Hubbard side bands [cf. black curve in Fig. 1(b)]. In sum, Hund physics is only observable at very low energy scales. Typical Mott physics, induced via the DMFT self-consistency, dominates.

Absence of Hund's coupling. For $J = 0$, SOS is absent: spin and orbital degrees of freedom are screened at the same scale, $T_{\mathrm{spin}} = T_{\mathrm{orb}}$ [cf. blue curves in Fig. 1(c)]. Far from the MIT phase boundary, e.g., for W0 with $J = 0$ and $\Delta_b = 3.5$ [marked by an open square in Fig. 1(a)], $T_{\mathrm{spin}} = T_{\mathrm{orb}} = 0.7405$ are rather large and

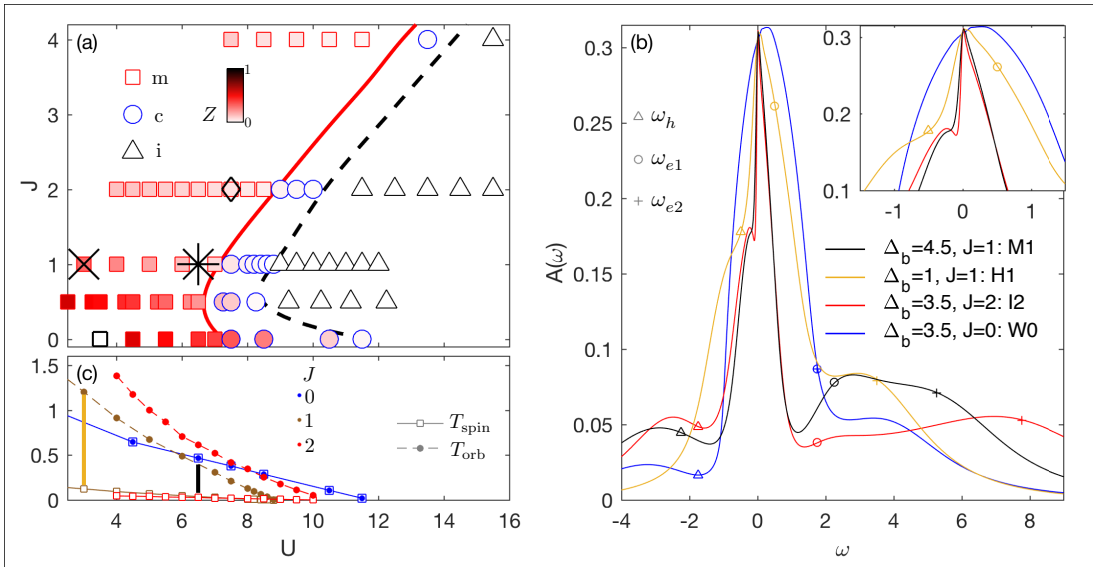

FIG. 1. (a) The zero-temperature phase diagram of the 3HHM has three phases in the J-U plane: a metallic phase (squares), a coexistence region (circles), and an insulating phase (triangles). These are separated by two phase transition lines U_{c1} (solid red curve) and U_{c2} (dashed black curve), respectively. The color intensity of the symbols in the metallic and coexistence regions indicates the value of $Z \in [0, 1]$: the lower Z the more faded is the red color. The phase diagram is adapted from Ref. [35]. We will present temperature-dependent results for a Hund system H1 far away from the U_{c1} phase transition line deep in the metallic state (cross), a Mott system M1 near the transition (asterisk), an intermediate system I2 having both Hund and Mott features (open diamond), and a weakly correlated system W0 with $J = 0$ far from U_{c1} (open square). (b) The local density of states $A(\omega)$ for M1 (black), H1 (yellow), I2 (red), and W0 (blue). The legend lists the corresponding values of the bare gap, $\Delta_b = U - 2J$. Triangles, circles, and crosses mark the bare atomic excitation scales, ω_h, ω_{e1}, and ω_{e2} (listed in increasing order), respectively, defined in Sec. III. The inset zooms into the peaks around the Fermi level $\omega = 0$. (c) The spin and orbital Kondo scales, $T_{\rm spin}$ (solid) and $T_{\rm orb}$ (dashed), plotted as function of U for $J = 0$ (blue), $J = 1$ (brown), and $J = 2$ (red); these scales are defined as the maxima of the imaginary parts of the dynamic orbital and spin susceptibilities, see Appendix A. The SOS window is marked by a vertical yellow (black) bar for H1 (M1).

thus $Z^{-1} = 1.5134$ not much enhanced: the system is only weakly correlated. The QP peak has no substructure [cf. blue curve in Fig. 1(b)].

Temperature-dependence. The size and the properties of the SOS window in frequency space has direct implications for temperature dependent properties of the 3HHM. This was first demonstrated in Ref. [7]. In particular, it was shown that, in local spectra, the QP peak persists up to very high temperatures in Hund systems, exhibiting large charge fluctuations, whereas a pseudogap develops with increasing temperature in all Mott systems at a characteristic energy scale $T_{\rm M}$, suppressing charge fluctuations. This can be explained by the fact that far from the MIT boundary the Hubbard bands overlap, whereas close to the boundary they are well separated. Furthermore, onset scales for orbital and spin screening, $T_{\rm orb}^{\rm onset}$ and $T_{\rm spin}^{\rm onset}$, were introduced as the scales where decreasing temperature first causes deviations of the respective static local orbital and spin susceptibilities, $\chi_{\rm orb}$ and $\chi_{\rm spin}$, from the Curie behavior, $\chi \propto 1/T$, characterizing free local moments. In Hund metals, it was found that $T_{\rm orb}^{\rm onset} \gg T_{\rm spin}^{\rm onset}$ with $T_{\rm orb}^{\rm onset}$ as high as $E_{\rm atomic}$. In contrast, in Mott systems, spin and orbital screening set in, simultaneously, below a much lower scale, $T_{\rm spin}^{\rm onset} \approx T_{\rm orb}^{\rm onset} \approx T_{\rm M} \ll E_{\rm atomic}$, together with the formation of the QP peak. A weakly correlated system with $J = 0$ likewise does not exhibit any separation of the onset scales of orbital and spin screening.

In addition, completion scales for orbital and spin screening, $T_{\rm orb}^{\rm cmp}$ and $T_{\rm spin}^{\rm cmp}$, were defined as the temperature scale below which Pauli behavior sets in with decreasing temperature. It was suggested that these scales are also separated in the presence of finite J in both Hund and Mott systems, while they are equal for $J = 0$ [7].

Strategy. In the following, we analyze and compare four different systems, H1, M1, W0 and I2, as presented in Fig. 1(a), to further clarify the Hund and Mott routes towards strong correlations. The Hund system, H1, and the Mott system, M1, are defined as in Ref. [7]. In addition, we also study the weakly correlated system W0 and an intermediate system I2 with $J = 2$ and $\Delta_b = 3.5$ [marked by an open diamond in Fig. 1(a)], which has both Hund and Mott features and thus demonstrates the crossover between Hund and Mott systems. For all these systems we summarize the physics in ARPES spectra at $T = 0$ and study their temperature dependencies. While some of this data is already presented as the Supplementary Information of Ref. [7], we here analyze it in much more detail and directly connect it to the temperature dependence of various other physical quantities. In particular, we revisit the static local susceptibilities and the idea of completion and onset scales of spin and orbital screen-

ing. Further insights are obtained by studying the quasiparticle weight, the resistivity, the thermopower, and the lattice entropy. We will show that the latter differs from the impurity entropy, studied before in Ref. [33]. In Appendix A, we also offer a detailed discussion, for I2, of the implications of particle-hole asymmetry for various frequency-dependent quantities at $T = 0$. All in all, these studies lead to a deepened understanding of the nature of Hund metals.

IV. ARPES, SPECTRAL FUNCTION, AND SELF-ENERGY

In this section we focus on ARPES spectra. We calculate the structure factor $A(\epsilon_k, \omega)$ for a Bethe lattice as

$$A(\epsilon_k, \omega) = -\tfrac{1}{\pi}\mathrm{Im}\left[\omega + \mu - \epsilon_k - \Sigma(\omega)\right]^{-1}. \qquad (4)$$

Experimentally, the structure factor can be measured by angle-resolved photoemission spectroscopy (ARPES). For brevity, our $A(\epsilon_k, \omega)$ spectra will be called ARPES spectra, too, although they are of course computed, not measured. The four Figs. 2, 4, 5, and 6 show our results for $A(\epsilon_k, \omega)$, together with the corresponding spectral function $A(\omega)$ and self-energy $\Sigma(\omega)$ for the four systems H1, M1, I2, and W0, respectively. $A(\epsilon_k, \omega)$ is plotted for different temperatures in panels (a),(c), and (e)–(h). $A(\omega)$ is plotted for several temperatures in panel (i), analogously, $\mathrm{Re}\,\Sigma(\omega)$ in panel (j), and $\mathrm{Im}\,\Sigma(\omega)$ in panel (k). In the following, we are particularly interested in how SOS is reflected in ARPES data at $T = 0$, and how it develops with increasing temperature in Hund systems compared to Mott systems. How can the emerging differences be explained and interpreted physically?

A. Hund system H1

Let us first analyze Fig. 2 for H1. Here, we start with the $T = 0$ results [Figs. 2(a) and 2(c)]. We reveal three regimes with different behavior of the ARPES spectrum, $A(\epsilon_k, \omega)$, due to SOS.

Fermi-liquid regime at $T = 0$. Figure 2(a) is a zoom into the FL regime, which at $T = 0$ sets in for $|\omega| < T_{\mathrm{spin}} = 0.1221$. The white curve shows the ω dispersion of the QP band, defined as the maxima $E^*(\omega)$ of $A(\epsilon_k, \omega)$ for given ω, and the blue curve the ϵ_k dispersion, defined as the maxima $E(\epsilon_k)$ of $A(\epsilon_k, \omega)$ for given ϵ_k. Both definitions lead to the same low-energy linear FL dispersion relation (cf. thick dashed red line) of slope $Z = 0.29$ [with a Fermi surface crossing point $E^*(\omega = 0) = \mu_{\mathrm{eff}}$]. The mass enhancement of the Landau QPs in the Hund system H1 is thus fairly large, $Z^{-1} = m^*/m = 3.45$. We define ω_{FL}^- and ω_{FL}^+ as the negative and positive crossover scales between which FL behavior holds [as diagnosed from a detailed analysis of the ω dependence of $A(\omega)$ and $\Sigma(\omega)$, see Appendix A for a detailed discussion]. Interestingly, we find that the extent of the FL regime is different for negative or positive frequencies, $\omega_{\mathrm{FL}}^- \neq \omega_{\mathrm{FL}}^+$ (cf. thin dash-dotted red horizontal lines): the white (blue) QP band dispersion deviates earlier from the thick dashed red FL line on the positive frequency side, i.e., at a lower scale $\omega_{\mathrm{FL}}^+ \approx -\frac{1}{3}\omega_{\mathrm{FL}}^- = 0.027$. The asymmetry of the FL regime directly reflects the particle-hole asymmetry of the model away from half-filling. The asymmetry of the FL regime is discussed in more detail in Appendix A. With $\omega_{\mathrm{FL}}^+ - \omega_{\mathrm{FL}}^- = 0.109$, the FL regime is rather large in H1 (compared to the lowest bare atomic excitation scale $E_{\mathrm{atomic}}^{\mathrm{H1}} = 0.5$). We remark that a similar asymmetric FL regime was found earlier in a one-band hole-doped Mott insulator [76], i.e., for a particle-hole asymmetric model with only one type of degrees of freedom (spins). There, it was also shown that a well-defined QP peak of "resilient" QP excitations exists at temperatures above the FL scale, and that it dominates an intermediate incoherent transport regime.

Crossover regime at $T = 0$. Above ω_{FL}^+ and below ω_{FL}^- the QP band starts to deviate from FL behavior and crosses over into the NFL regime. In this regime, the dispersion relation becomes highly particle-hole asymmetric, as clearly visible in Fig. 2(c). For $\omega > 0$, E (and E^*) turn upwards with increasing ϵ_k into a steeper approximately linear function. This crossover is reflected in a weak kink around a crossover scale $\omega_{\mathrm{cr}}^+ = 0.085$ (solid yellow line at $\omega > 0$). For $\omega < 0$, E develops into a step-shaped curve for decreasing ϵ_k approximately at the crossover scale $\omega_{\mathrm{cr}}^- = -0.256$ (solid yellow line at $\omega < 0$). By contrast, E^* essentially keeps following the red FL line almost down to ω_{cr}^-, before a jump signals the transition to a new type of transport regime, the HQP regime, where HQP stands for "Hund quasiparticle", explained further below.

HQP regime at $T = 0$. For ω below the above-mentioned jump, i.e., well smaller than crossover scale $-\omega_{\mathrm{cr}}^-$, the ω dispersion $E^*(\omega)$ (white line) approaches the steep linear behavior of the ϵ_k dispersion $E(\epsilon_k)$ (blue line). Thus, the dispersion in the HQP regime is again linear, similar to the FL regime, but it is steeper than in the latter, for both negative and positive ω. This signals the survival of resilient but lighter QPs in the HQP regime, described in more detail below. Interestingly, the slope of E (E^*) is slightly larger for negative ($\omega < -\omega_{\mathrm{cr}}^-$) than for positive ($\omega > \omega_{\mathrm{cr}}^+$) frequencies, indicating different effective masses for electrons and holes.

SOS Kondo screening process. We can now establish a connection between the three different frequency regimes identified above in the ARPES spectrum, and the intertwined two-stage Kondo screening process of SOS (cf. Fig. 3) analyzed in Refs. [7, 33, 35]. Proceeding from high to low frequencies (energies), orbital screening sets in first. This involves the formation of an orbital singlet, by binding one bath electron to the impurity to screen the orbital hole. Due to Hund's coupling, the extra bath electron couples ferromagnetically to the impurity, leading

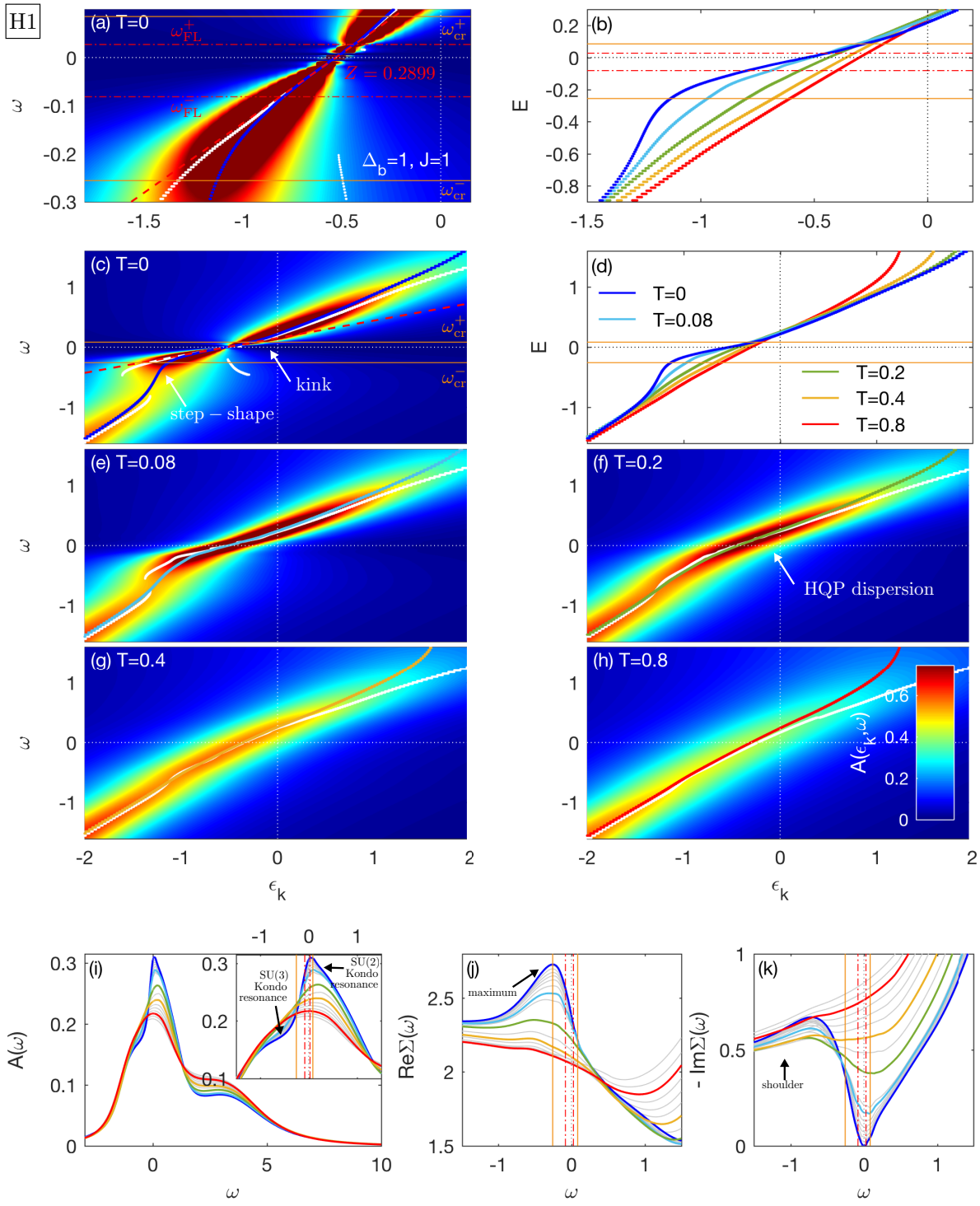

FIG. 2. A Hund system (H1) with parameters $\Delta_b = 1$ and $J = 1$. [(a),(c),(e)–(h)] The structure factor $A(\epsilon_k, \omega)$. [(b),(d)] The dispersion relation $E(\epsilon_k)$, (i) the spectral function $A(\omega)$, [(j),(k)] the real and imaginary parts of the self-energy, $\mathrm{Re}\,\Sigma(\omega)$ and $\mathrm{Im}\,\Sigma(\omega)$, respectively, all plotted for various temperatures. [(a),(c),(e)–(h)] The colored curves highlight the dispersion relation $E(\epsilon_k)$ and the white curves show the alternative definition of the dispersion relation $E^*(\omega)$. Panels (a) and (b) are low-energy zooms of panels (c) and (d). The FL regime, $\omega_{\mathrm{FL}}^- < \omega < \omega_{\mathrm{FL}}^+$, lies between the dash-dotted red lines, running horizontally in (a) and (b) and vertically in (i)–(k). The thick dashed red line in panel (a) denotes FL behavior of the low-energy dispersion relation. Its slope $Z = m/m^*$ reflects the strength of local correlations. The yellow solid horizontal lines in (b) and vertical lines in (i)–(k) denote, for $\omega < 0$, the energy scale ω_{cr}^- of the maximum in $\mathrm{Re}\,\Sigma_{T=0}(\omega < 0)$, and for $\omega > 0$, the energy scale ω_{cr}^+ of the kink in $\mathrm{Re}\,\Sigma_{T=0}(\omega > 0)$.

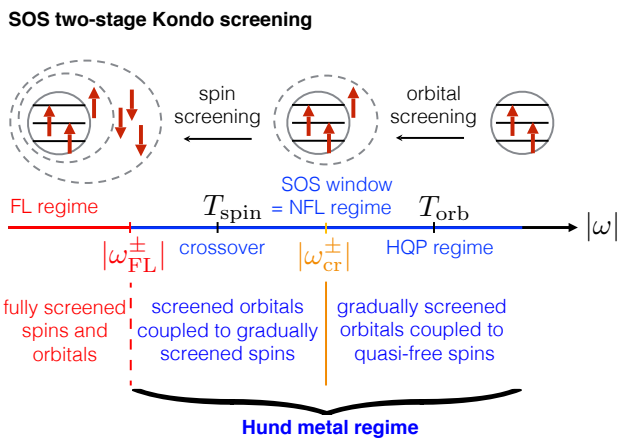

FIG. 3. Refined schematic depiction of the two-stage Kondo screening process of SOS at filling $n_d = 2$ (based on Fig. 13 of Ref. [35]). With decreasing energy orbital screening sets in first, roughly at the orbital Kondo scale $T_{\rm orb}$. This involves the formation of an orbital singlet by building a large effective Hund's-coupling-induced 3/2 spin including a bath spin degree of freedom. $|\omega^{\pm}_{\rm cr}|$ approximately marks the completion of orbital screening. Below $|\omega^{\pm}_{\rm cr}|$ the 3/2 spin is gradually screened by the three effective channels of the 3HHM. Well below the spin Kondo scale $T_{\rm spin}$, full screening of both orbital and spin degrees of freedom is reached at the FL scale $|\omega^{\pm}_{\rm FL}|$, below which FL behavior occurs in frequency-dependent quantities. Our schematic sketch ignores the effects of particle-hole asymmetry on the crossover scales, $|\omega^{-}_{\rm cr}| \neq |\omega^{+}_{\rm cr}|$ and $|\omega^{-}_{\rm FL}| \neq |\omega^{+}_{\rm FL}|$.

to the emergence of a large effective 3/2 impurity spin. This transport regime has NFL properties, but is characterized by an ARPES spectrum with a surprisingly linear band dispersion, having a much steeper slope, i.e., a much smaller mass enhancement, than in the FL regime. It might thus be described in terms of specific resilient QPs, which are formed by gradually screened orbital degrees of freedom coupled to quasi-free large spins. We dub these resilient QPs "Hund quasiparticles" (HQPs). The steep slope of this HQP band (especially at negative frequencies) is reminiscent of the (inverted) waterfall structure discovered in ARPES spectra and realistic density functional theory (DFT) plus quantum Monte Carlo (QMC) studies of Sr_2RuO_4 [77]. We thus corroborate the suggestion of Ref. [77] that the waterfall structure is a signature of resilient QPs in Hund metals. But we also remark that a waterfall structure was also found in ARPES plots for the hole-doped one-band Hubbard model in Ref. [76]. The "completion" of the orbital screening process is reflected in a (strong) change in the band dispersion around $\omega^{-}_{\rm cr}$ (step-shape) and $\omega^{+}_{\rm cr}$ (kink), respectively. Notably, subtle changes (kinks) at about 30 meV were reported in ARPES data of Sr_2RuO_4 [22, 77, 78], presumably caused by local electronic correlations [78], and therefore could be associated with the crossover from the NFL to the FL regime. For frequencies below $\omega^{+}_{\rm cr}$ and above $\omega^{-}_{\rm cr}$ spin screening sets in: the large 3/2 spin is now screened by the three channels of the 3HHM to additionally form a spin singlet in the ground state. Figuratively speaking the HQPs get additionally dressed by the spin degrees of freedom. After completion, FL behavior characterizes the low-frequency regime. Here, the QP band can be described in terms of Landau QPs with a heavy mass $Z^{-1} = m^*/m$, reflected by the small slope Z of the band dispersion in ARPES data. These Landau QPs are more stable on the negative frequency side.

As has been discussed in Sec. III and Refs. [33, 35], the two-step screening process of SOS is also reflected in $A(\omega)$ and $\Sigma(\omega)$. In $A(\omega)$ a narrow SU(2) spin Kondo peak sits on top of a broad SU(3) orbital Kondo peak [cf. blue curve in Fig. 2(i)], resulting in a shoulder for $\omega < \omega^{-}_{\rm cr}$ and a subtle kink for $\omega > \omega^{+}_{\rm cr}$ (cf. vertical solid yellow lines). Correspondingly, $-\mathrm{Im}\,\Sigma(\omega)$ [cf. blue curve in Fig. 2(k)] develops a shoulder below $\omega^{-}_{\rm cr}$ and a regime above $\omega^{+}_{\rm cr}$ in which the slope of $-\mathrm{Im}\,\Sigma(\omega)$ becomes smaller than for $\omega < \omega^{+}_{\rm cr}$. The scattering rate in the HQP regime is thus less energy dependent than in the FL regime. The shoulder-like structure in $-\mathrm{Im}\,\Sigma(\omega < 0)$ directly translates to a sharp maximum in $\mathrm{Re}\,\Sigma(\omega < 0)$ [cf. blue curve in Fig. 2(j)]. We use the position of this maximum to define $\omega^{-}_{\rm cr}$ (vertical solid yellow line at $\omega < 0$). The kink in $\mathrm{Re}\,\Sigma(\omega > 0)$ approximately marks $\omega^{+}_{\rm cr}$ (vertical solid yellow line at $\omega > 0$), which turns out to lie at $\frac{1}{3}\omega^{-}_{\rm cr}$. While these scales are in principle heuristic choices, their physical relevance can be motivated by the fact that they directly reflect the energy scales of marked changes in the band dispersion $E(\epsilon_k)$: the latter is the solution to the equation $\omega + \mu - \epsilon_k - \mathrm{Re}\,\Sigma(\omega) = 0$, as used in Ref. [6], and thus directly connected to $\mathrm{Re}\,\Sigma(\omega)$. In Appendix A, we complement this discussion by a detailed investigation of the frequency dependence of $A(\omega)$, $\Sigma(\omega)$, and the dynamical spin and orbital susceptibilities, $\chi_{\rm spin}(\omega)$ and $\chi_{\rm orb}(\omega)$, at $T = 0$ for the system I2 and their interpretation in terms of the SOS screening process.

We remark that the SOS features described above, in particular the shoulder below $\omega^{-}_{\rm cr}$ in both $A(\omega)$ and $-\mathrm{Im}\,\Sigma(\omega)$, have also been predicted to occur for Sr_2MoO_4 in very recent DFT+DMRG studies [40].

Temperature dependence. In order to verify the idea of robust HQPs governing the incoherent transport regime, we study the evolution of the QP band and its dispersion E with temperature in Figs. 2(c), 2(e)–2(h) and Figs. 2(b) and 2(d), respectively. We find that, with increasing temperature, first the SOS features in the dispersion, like the step at $\omega < 0$ and the kink at $\omega > 0$, dissolve gradually and very slowly, while the steep slope of the linear behavior characteristic of the HQP regime remains unchanged [cf. Fig. 2(d)]. At $T \gtrsim 0.2$ the Landau-FL QP band has fully disappeared and only a slight kink at the Fermi level separates the linear parts of the resilient HQP band at $\omega > 0$ and $\omega < 0$ [cf. green curves in Figs. 2(b), 2(d), and 2(f)]. The slope of the HQP band remains quite stable over a very broad range of frequencies (especially for $\omega < 0$) up to the highest temperature plotted [cf. Fig. 2(d)]. Thus the incoherent transport

regime for $T \gtrsim 0.2$ is governed by a very robust, almost temperature independent HQP band.

This evolution of the QP band with increasing temperature is also reflected in $A(\omega)$, $\mathrm{Re}\,\Sigma(\omega)$, and $\mathrm{Im}\,\Sigma(\omega)$ [cf. Figs. 2(i)–2(k)]. In the FL temperature regime a sharp SU(2) Kondo peak in $A(\omega)$, a pronounced maximum in $\mathrm{Re}\,\Sigma(\omega)$, and a shoulder and dip in $\mathrm{Im}\,\Sigma(\omega)$ are clearly visible (cf. blue curves). With increasing temperature there is a gradual crossover to NFL behavior. The height of the SU(2) Kondo resonance in $A(\omega)$ decreases and the two-tier structure of the QP peak disperses by redistributing spectral weight from the SU(2) Kondo peak to the SU(3) Kondo resonance shoulder. However, the width of the broad SU(3) Kondo resonance is essentially unaffected by this redistribution. In fact, the robustness of the HQP band is reflected in the stable form of the QP peak flank of $A(\omega)$, especially at negative frequencies [cf. Fig. 2(i)]. Interestingly, this flank is stabilized by the lower Hubbard band, which lies around $\omega_h = -0.5$, i.e., the SU(3) Kondo resonance and atomic excitations merge in H1, resulting in a robust ARPES spectrum with mixed valence character at very high temperatures [7].

Next we consider the self-energy. Reflecting the temperature dependence of $A(\omega)$, also the maximum in $\mathrm{Re}\,\Sigma(\omega)$ and the dip and the shoulder in $\mathrm{Im}\,\Sigma(\omega)$ get first gradually smeared out with increasing temperature for $T \lesssim 0.2$. Notably, the minimum of $-\mathrm{Im}\,\Sigma(\omega, T)$ is shifted to positive frequencies within this process. This hints towards long-lived electron-like excitations governing the incoherent transport of this crossover regime. The minimum in $-\mathrm{Im}\,\Sigma(\omega, T)$ disappears at higher temperatures and $-\mathrm{Im}\,\Sigma(\omega, T)$ becomes a monotonically increasing function of frequency close to the Fermi level. This might again be caused by mixed valence physics, which becomes important at an energy scale of around 0.5.

Interestingly, very similar behavior of the minimum of $-\mathrm{Im}\,\Sigma(\omega, T)$ is observed for the hole-doped one-band Hubbard model of Ref. [76]. There, a well-defined QP peak persists with increasing temperature above the coherence scale until it merges with the lower Hubbard band at high temperatures.

Note that the temperature dependence of $\mathrm{Re}\,\Sigma(\omega)$ directly determines the temperature dependence of the dispersion relation $E(\epsilon_k)$ in $A(\epsilon_k, \omega)$ [cf. Fig. 2(d)]. Again, the evolution of the QP band with temperature strongly hints towards the existence of different types of QPs. At very low T in the FL regime, the band is described by a low-frequency FL-like QP band with a rather flat dispersion. Correspondingly, $A(\omega)$ exhibits a sharp SU(2) Kondo resonance. Then, with increasing temperature, a crossover takes place: The low-frequency FL-like QP band dissolves gradually until, at higher temperatures, we find a new QP regime, the HQP regime. There, a much steeper (slightly particle-hole asymmetric) HQP band exists and the two-tier QP peak in $A(\omega)$ is reduced to a single broad resilient SU(3) Kondo resonance.

B. Mott system M1

We now turn to the Mott system M1. Figure 4 displays its spectral properties using the same layout as Fig. 2 for H1. At $T = 0$ we again find a particle-hole asymmetric FL frequency regime and SOS features [cf. Figs. 4(a) and 4(c)]. However, these occur at much lower frequencies than in H1 (for instance, M1 has $\omega_{\mathrm{cr}}^{-} = -0.15$), as expected from the insights given in Sec. III. The slope of the FL dispersion $Z = 0.10$ is clearly smaller for M1 than for H1, indicating much heavier electron masses. With increasing temperature, the SOS features vanish very quickly (already below $T = 0.08$ for M1) [cf. Figs. 4(b) and 4(d)]. The emergent HQP band [cf. Fig. 4(f)] is very unstable with increasing temperature and already starts to disappear at around $T = 0.15$ [cf. Figs. 4(d) and 4(g)]. Above $T \gtrsim 0.2$ a pseudogap has fully replaced the QP peak [cf. Figs. 4(h)]. Similarly, the whole QP peak in $A(\omega)$ becomes strongly suppressed, eventually turning into a pseudogap at high temperatures [red curve in Fig. 4(i)]. The emergence of a pseudogap is accompanied by a change of sign, from positive to negative, in the slope of the dispersion relation $E(\epsilon_k)$ [cf. red curve in Fig. 4(d)]. Consequently, $\mathrm{Re}\,\Sigma(\omega)$ and $\mathrm{Im}\,\Sigma(\omega)$ are strongly temperature dependent, as well. While for $T \lesssim 0.08$ the minimum of $-\mathrm{Im}\,\Sigma(\omega, T)$ is shifted to positive frequencies, it is gradually shifted back towards negative frequencies with increasing temperature and finally turns over to a maximum in the presence of a pseudogap [cf. Fig. 4(k)].

C. Intermediate system I2

Figure 5 shows spectral data for the intermediate system I2. At $T = 0$, the ARPES spectrum for I2 [cf. Figs. 5(a) and 5(c)] shows SOS features similar to those of H1, but occurring at smaller scales. Since $J = 2$ and the bare gap $\Delta_b = 3.5$ are both large, T_{spin} is pushed down [35] even compared to M1: $T_{\mathrm{spin}} = 0.021$ and thus $Z = 0.055$ (cf. thick dashed red line) but also $|\omega_{\mathrm{FL}}^{\pm}|$ and $|\omega_{\mathrm{cr}}^{\pm}|$ take approximately half the values of the respective scales of M1, while $T_{\mathrm{orb}} = 0.42$ for I2 is slightly larger than $T_{\mathrm{orb}} = 0.3878$ for M1. In sum, the zero-temperature band dispersion of I2 is similar in its shape to H1 and M1.

However, qualitative differences emerge in the temperature evolution of the QP band and its dispersion E compared to H1 and M1, respectively—again due to the specific relation $[T_{\mathrm{spin}}, T_{\mathrm{orb}}]/\Delta_b$ for I2. With increasing temperature, first the band's step-shaped structure gradually dissolves, while its steep linear behavior in the HQP frequency regime remains unchanged [cf. bright blue curve for $T = 0.02$ in Figs. 5(b), 5(d), and Fig. 5(e)]. In contrast to M1, this HQP band is stable up to rather high temperatures, $T = 0.25$, for I2 (similar to H1). Nevertheless, above $T = 0.25$, we additionally find a crossover to a pseudogap similar to M1 [cf. red curves in Figs. 5(b),

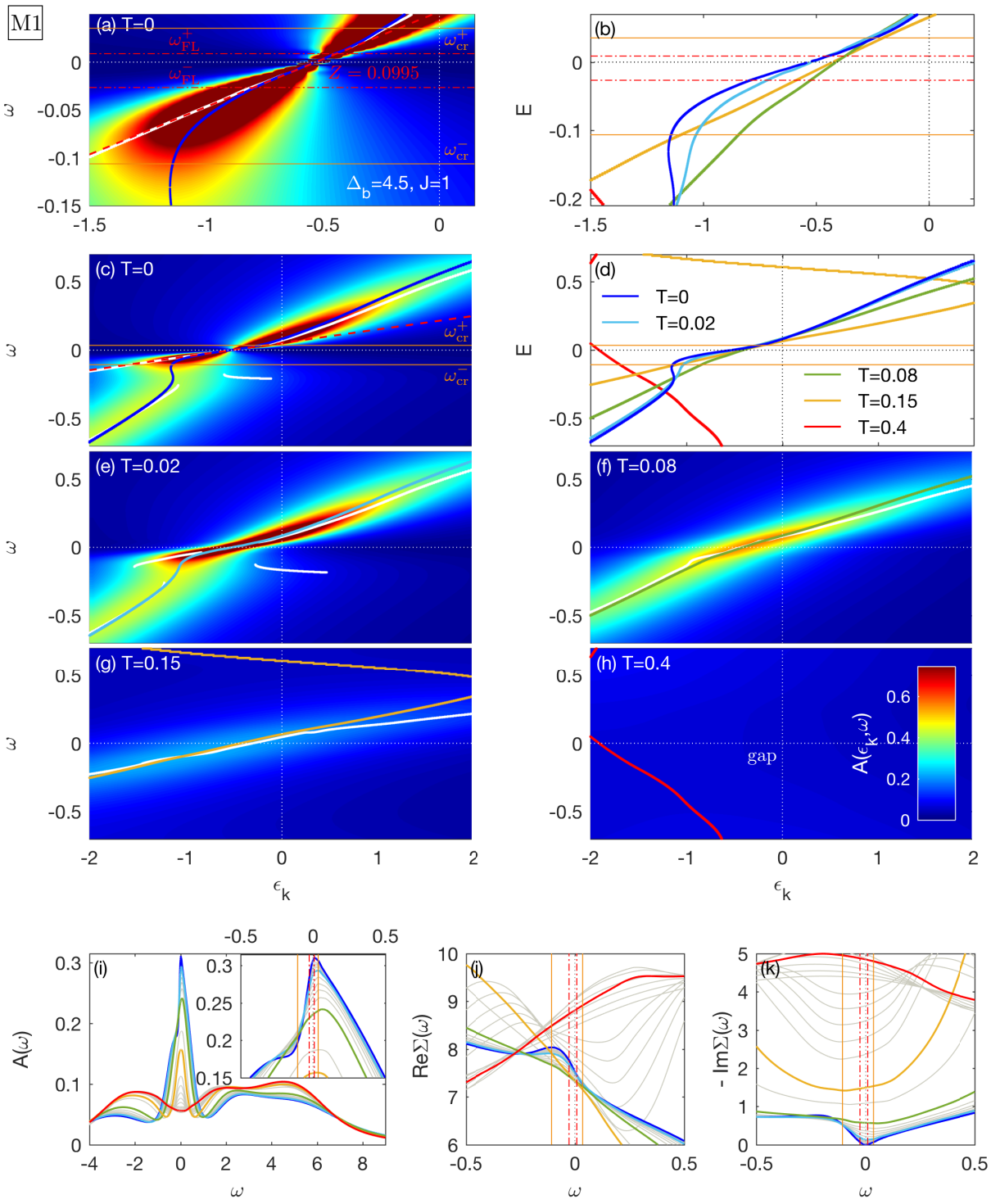

FIG. 4. Same quantities as in Fig. 2 for a Mott system (M1) with parameters $\Delta_b = 4.5$ and $J = 1$.

5(d), 5(h), and 5(i)]. I2 is thus characterized by both a Hund feature (HQP band) at intermediate temperatures and a Mott feature (pseudogap) at very high temperatures. This evolution of the QP band with temperature is again reflected in $A(\omega)$, $\mathrm{Re}\,\Sigma(\omega)$, and $\mathrm{Im}\,\Sigma(\omega)$ [cf. Figs. 5(i)–5(k)].

D. Weakly correlated system W0

For $J = 0$ the SOS features are fully absent in $A(\epsilon_k, \omega)$, $A(\omega)$, $\mathrm{Re}\,\Sigma(\omega)$, and $\mathrm{Im}\,\Sigma(\omega)$ (cf. Fig. 6). The FL behavior holds for a rather large temperature regime (almost

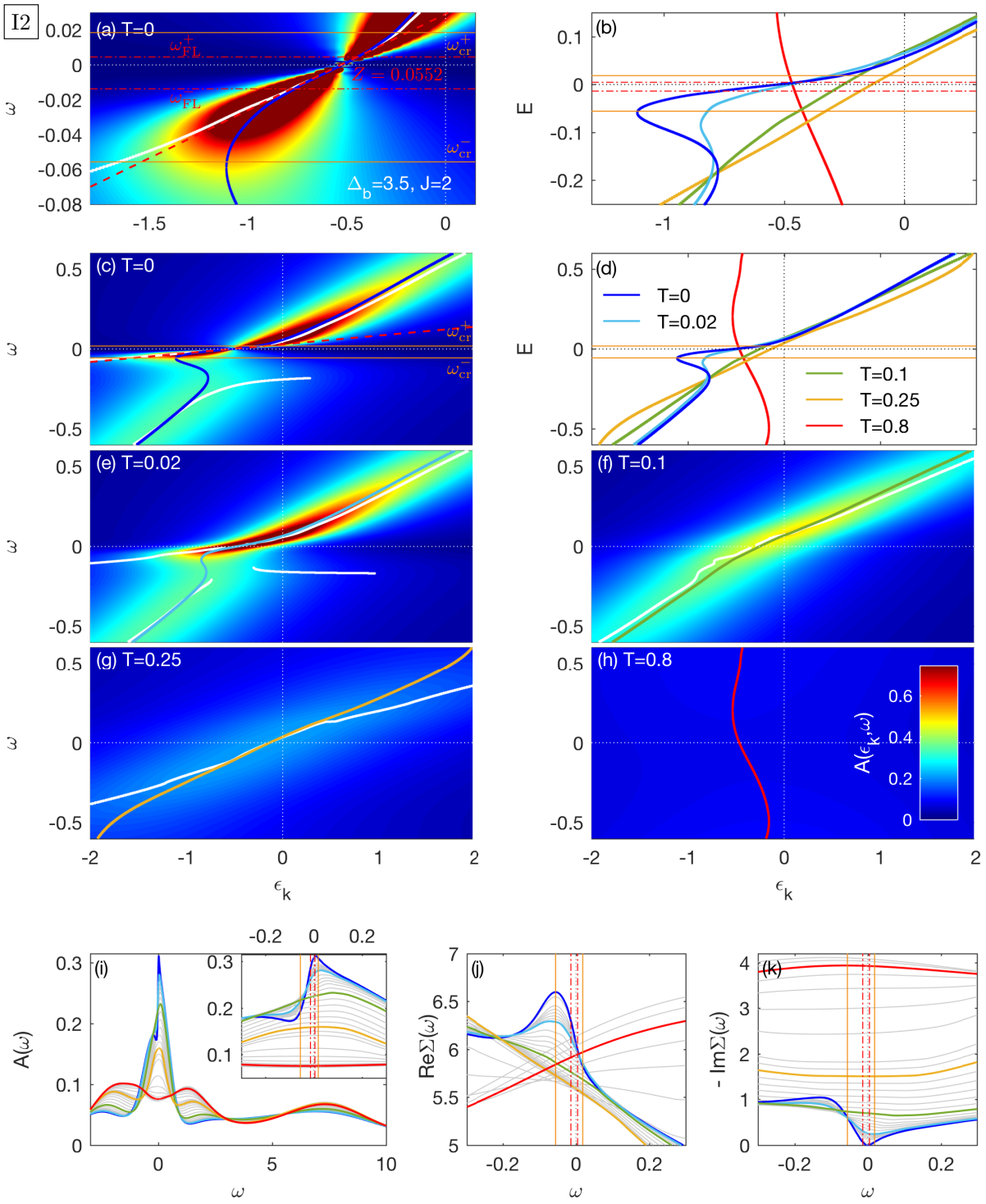

FIG. 5. Same quantities as in Fig. 2 for an intermediate system (I2) with paramters $\Delta_b = 3.5$ and $J = 2$.

up to $T \approx 0.25$) and is characterized by a very stable large dispersion with $Z = 0.6672$ and thus a rather small mass enhancement. Resilient HQPs do not exist.

E. Summary of spectral properties

To summarize, both H1 and M1 (and also I2) show SOS features in the dispersion extracted from $A(\epsilon_k, \omega)$ at $T = 0$: (i) a rather flat low-frequency Landau QP band of slope Z; (ii) a NFL crossover behavior (in form of a

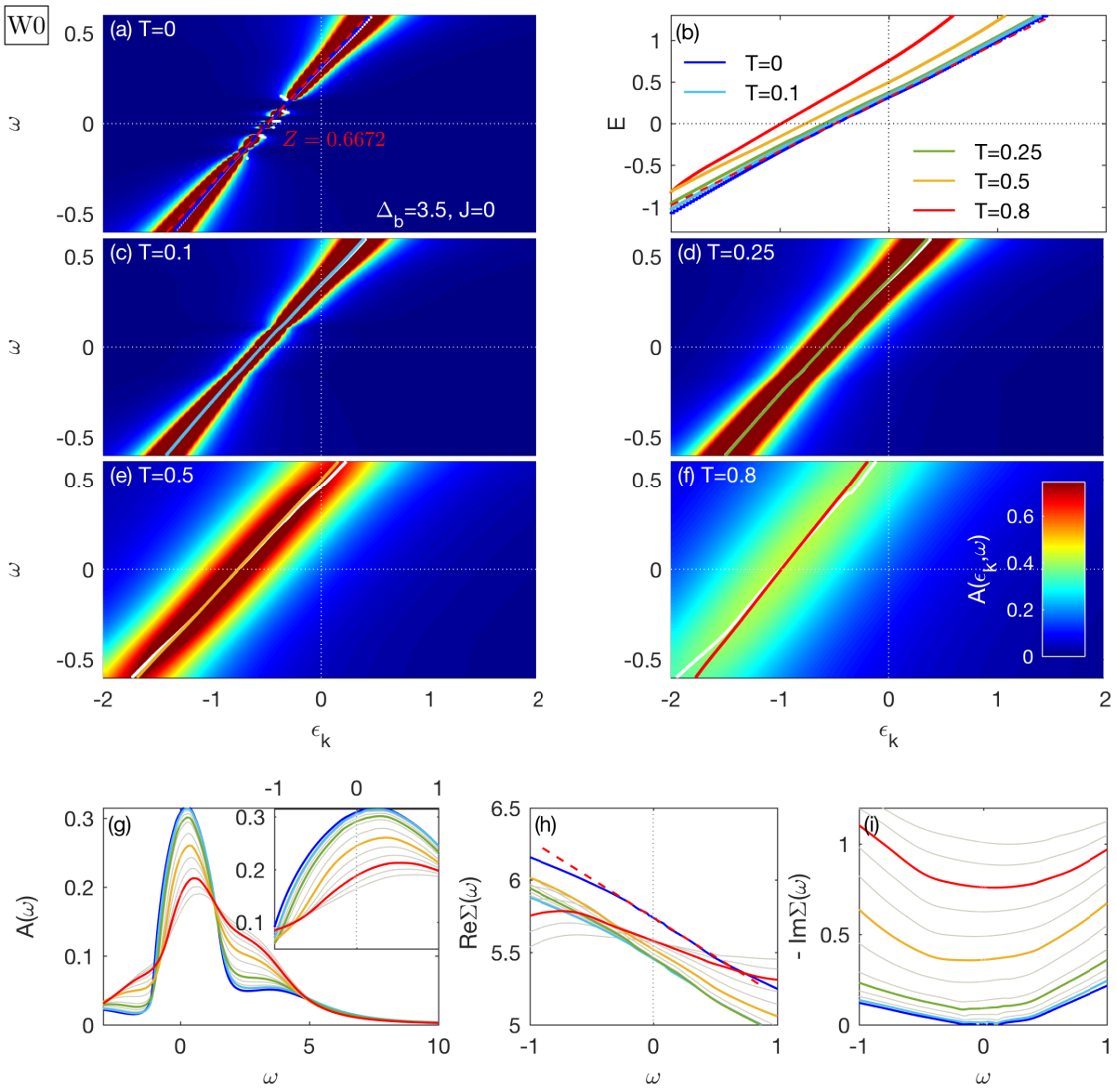

FIG. 6. A weakly coupled system W0 with parameters $\Delta_b = 3.5$ and $J = 0$. [(a),(c)–(f)] The structure factor $A(\epsilon_k, \omega)$. (b) The dispersion relation $E(\epsilon_k)$, (g) the spectral function $A(\omega)$, [(h),(i)] the real and imaginary parts of the self-energy, $\mathrm{Re}\,\Sigma(\omega)$ and $\mathrm{Im}\,\Sigma(\omega)$, respectively, all plotted for various temperatures. (h) Note that the difference in $\mathrm{Re}\,\Sigma(\omega = 0)$ between $T = 0$ and $T > 0$ arises from a 4% deviation of $n_d(T = 0)$ from $n_d = 2$. FL and crossover scales are not shown. Note that the latter do not exist for $J = 0$.

step-shaped band at $\omega < 0$ and a kink at $\omega > 0$); and (iii) a HQP band, which is extended in frequency space. The latter consists of positive and negative frequency parts, both of which exhibit linear dispersion relations with large slopes, with the negative-frequency slope slightly larger than the positive-frequency slope. However, these SOS features occur at very different energy scales for the three systems [35]: while in H1 they are extended over a broad frequency range up to atomic energy scales, they are compressed and lie at smaller frequency scales in M1. Consequently, in H1, these features govern transport for all temperatures. In particular, very robust HQPs exist up to the highest ($\lesssim t$) temperatures. By contrast, in M1, SOS physics only survives at very low temperatures, whereas the behavior of $A(\epsilon_k, \omega)$ at higher temperatures is dominated by typical Mott physics, i.e., the DMFT self-consistency opens a (pseudo)gap and quickly destroys the HQPs. For I2, the SOS features are also found at rather low scales (due to the large Δ_b) at $T = 0$, but the SOS regime is more extended than for M1 (due to the large J). Temperature-dependent ARPES spectra thus show both Hund and Mott features. If $J = 0$, SOS features are absent and W0 is governed by FL behavior in a broad temperature range.

V. STATIC LOCAL ORBITAL AND SPIN SUSCEPTIBILITIES, AND QUASIPARTICLE WEIGHT

Based on the above detailed analyzis of the ARPES spectra, we now revisit the static local susceptibilities for the orbital and spin degrees of freedom, to refine the findings which we had reported in Ref. [7]. There we introduced four temperature scales, characterizing the onset and the completion of screening of the spin and the orbital degrees of freedom. The concept of onset and completion scales for screening was inspired by Wilson's classic analysis of the impurity contribution to the spin susceptibility of the spin-1/2 one-channel Kondo model, reviewed in Appendix B. We correspondingly derived these scales from the behavior of the static local spin and orbital susceptibilities, and also of the local spectral function. Our main result was that Hund and Mott systems show contrasting behavior at intermediate to high energies. In Hund systems, we found a clear separation in the energy scales at which the screening for orbital and spin fluctuations sets in, respectively: $T_{\rm orb}^{\rm onset} \gg T_{\rm spin}^{\rm onset}$, with $T_{\rm orb}^{\rm onset}$ very large ($\gtrsim E_{\rm atomic}$). By contrast, in Mott systems the strong Coulomb repulsion localizes the charge at high temperature. With decreasing temperature the onset of charge localization triggers the simultaneous onset of the screening of the spin and orbital degrees of freedom, accompanied by the formation of the coherence resonance at $T_{\rm M} \equiv T_{\rm spin}^{\rm onset} = T_{\rm orb}^{\rm onset} \ll E_{\rm atomic}$. At low temperatures, we suspected SOS in the completion of screening, $T_{\rm orb}^{\rm cmp} \gg T_{\rm spin}^{\rm cmp}$, both for Hund and Mott systems, but considered this to be more pronounced for Hund systems.

In this section we now reanalyze the static local susceptibilities of H1 and M1 of Ref. [7]. While we only slightly refine the onset scales of screening quantitatively to provide a clearer connection to corresponding ARPES data and the quasiparticle weight, we suggest a revised perspective on the completion scales. In sum, we establish a consistent physical picture of screening from the atomic degrees of freedom at high energies to the quasiparticles at low energies. We corroborate our findings by studying the static local susceptibilities of I2 and W0.

The dynamical real-frequency spin and orbital susceptibilities are defined as

$$\chi^{\rm spin}(\omega) = \tfrac{1}{3}\sum_{\alpha}\langle \hat{S}^{\alpha}\|\hat{S}^{\alpha}\rangle_{\omega}, \tag{5a}$$

$$\chi^{\rm orb}(\omega) = \tfrac{1}{8}\sum_{a}\langle \hat{T}^{a}\|\hat{T}^{a}\rangle_{\omega}, \tag{5b}$$

respectively [71, 79], where $\hat{T}^a = \sum_{mm'\sigma} \hat{d}^{\dagger}_{m\sigma}\frac{1}{2}\tau^a_{mm'}\hat{d}_{m'\sigma}$ are the impurity orbital operators with the SU(3) Gell-Mann matrices τ^a normalized as $\mathrm{Tr}[\tau^a\tau^b] = 2\delta_{ab}$. Below the subscript 0 will be used to denote the static limit, $\chi_0 = \chi(\omega = 0)$, i.e., the static local susceptibilities.

We plot $T\chi_0^{\rm orb,spin}$ in Figs. 7(a), 7(b), 7(e), and 7(f) and $\chi_0^{\rm orb,spin}$ in Figs. 7(c), 7(d), 7(g), and 7(h) as functions of T, for H1 (yellow), M1 (black), I2 (red), and W0 (blue). As a function of decreasing temperatures, these susceptibilities traverse four regimes: first Curie-like behavior, where $T\chi_0$ is independent of temperature; onset of screening, where $T\chi_0$ begins to decrease; completion of screening, where χ_0 begins to saturate; and Pauli behavior, where χ_0 is constant. We will discuss these regimes in detail below.

We also plot the quasiparticle weight $Z(T)$ as dotted lines in Figs. 7(a), 7(b), 7(e), and 7(f) [and additionally in Figs. 9(a) and 9(b)]. In principle, the interpretation of $Z(T)$ as quasiparticle weight holds only in the FL regime. Nevertheless, for temperatures in the NFL regime, it is still computationally well-defined and we use it to interpret the physics on a heuristic level.

A. Hund system H1

We begin with a discussion of the results for H1 in Figs. 7(a)–7(d). $T\chi_0^{\rm orb}$ decreases with decreasing temperature for all temperatures plotted [cf. dashed yellow curves in Figs. 7(a) and 7(b)], i.e., the onset for orbital screening, $T_{\rm orb}^{\rm onset} > 1$, is on the order of bare excitation scales. The onset of spin screening, $T_{\rm spin}^{\rm onset} \approx 0.25$, is signaled by the deviation from Curie-like (constant) behavior of $T\chi_0^{\rm spin}$ with decreasing temperature, marked by the yellow triangle [cf. solid yellow curves in Figs. 7(a) and 7b)]. Thus, for H1, we find $T_{\rm orb}^{\rm onset} \gg T_{\rm spin}^{\rm onset}$, as shown in Ref. [7]. Note, however, that here we have chosen $T_{\rm spin}^{\rm onset} \approx 0.25$ slightly smaller than in Ref. [7] (where we had chosen $T_{\rm spin}^{\rm onset} \approx 0.4$). This choice is motivated by the ARPES data in Fig. 2. There the onset of spin screening is reflected in the formation of a flat low-frequency band in addition to the steep HQP band, resulting in a pronounced step-like feature in the dispersion at $T = 0$. In Fig. 2(d) the onset of the step formation is visible for $T \lesssim 0.2$. Furthermore, we motivate our choice in terms of the behavior of $\chi_0^{\rm orb}$. With $T_{\rm spin}^{\rm onset} \approx 0.25$, the onset scale of spin screening is equal to the temperature scale for the completion of orbital screening: $\chi_0^{\rm orb}$ shows Pauli (constant) behavior for $T < T_{\rm spin}^{\rm onset} \approx T_{\rm orb}^{\rm cmp}$ [cf. dashed yellow curve in Figs. 7(c) and 7(d)]. When the temperature is further lowered, $\chi_0^{\rm spin}$ too reaches Pauli behavior at $T_{\rm FL} = T_{\rm spin}^{\rm cmp}$ (yellow cross). Then spin screening is completed and the system is a FL.

Figure 8(a) summarizes these observations in a schematic sketch. In a Hund system, the SOS screening process of Fig. 3 is directly reflected in the temperature dependence of the static local susceptibilities. For $T_{\rm spin}^{\rm onset} < T < T_{\rm orb}^{\rm onset}$, HQPs, i.e., gradually screened (quasi-itinerant) orbitals coupled to quasi-free spins, dominate the physics and lead to a robust HQP band in ARPES spectra and a Curie-like spin susceptibility. At very high temperatures mixed-valence physics additionally comes into play [7], because the lower (and a part of the upper) Hubbard band merge at $\omega_h = -0.5$ (and

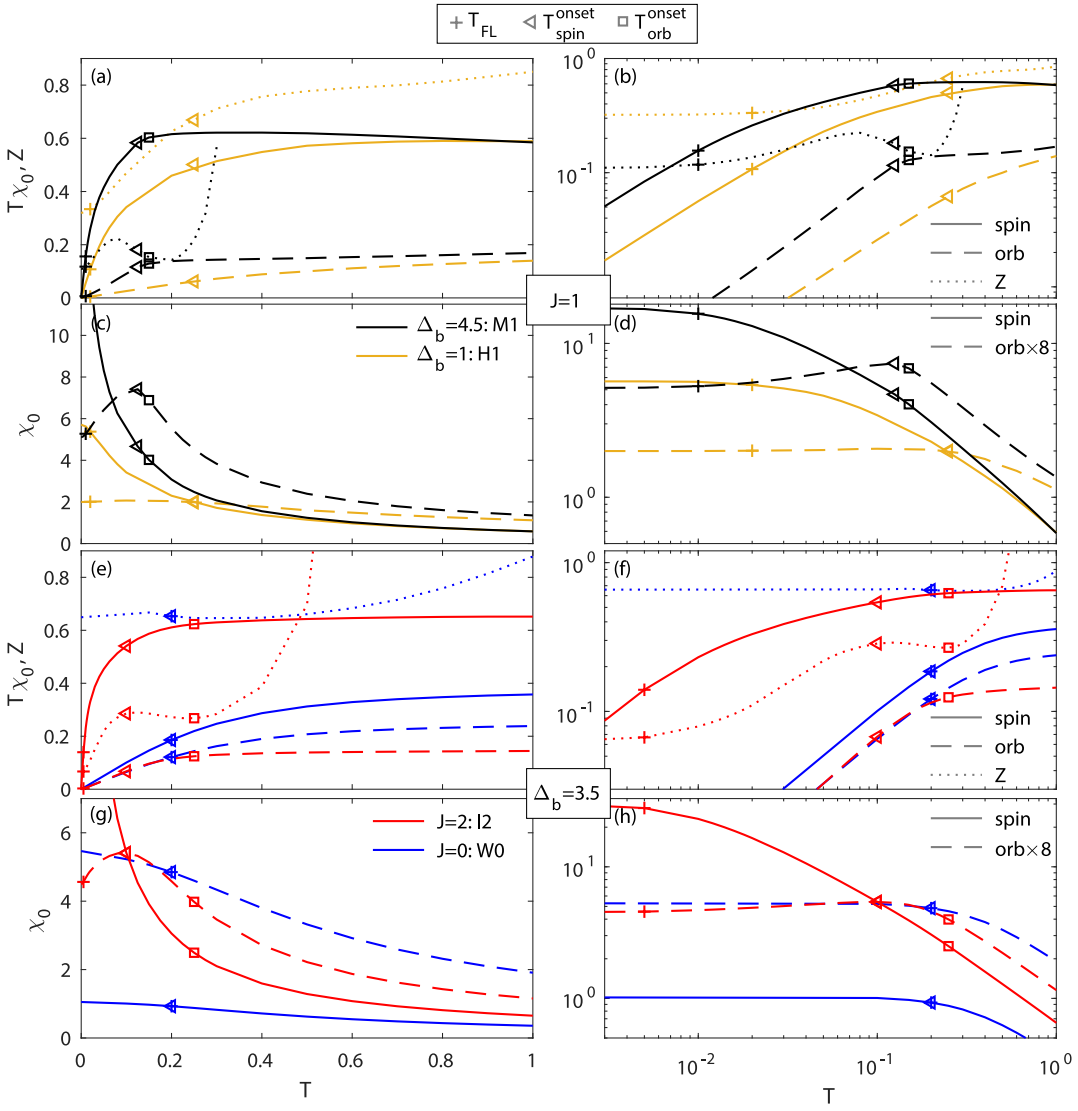

FIG. 7. The static local orbital (dashed) and spin (solid) susceptibilities, [(a),(b),(e),(f)] $T\chi^{\mathrm{orb,spin}}$ and [(c),(d),(g),(h)] $\chi_0^{\mathrm{orb,spin}}$, all plotted as functions of temperature on a linear (left) and a logarithmic (right) scale, for M1 (black), H1 (yellow), I2 (red), and W0 (blue). In addition, the quasiparticle weight (dotted) $Z(T)$ is shown in (a), (b), (e), and (f). The squares mark the onset of orbital screening $T_{\mathrm{orb}}^{\mathrm{onset}}$ below which $T\chi_0^{\mathrm{orb}}$ deviates from a constant value, i.e., from Curie-like behavior. Note that $Z(T)$ diverges for $T > T_{\mathrm{orb}}^{\mathrm{onset}}$. The triangles mark the maxima of χ_0^{orb} and also signal the onset of spin screening $T_{\mathrm{spin}}^{\mathrm{onset}}$ below which $T\chi_0^{\mathrm{spin}}$ deviates from Curie-like behavior. The crosses denote the FL scale T_{FL} below which FL behavior is found. In M1, we observe that $T_{\mathrm{spin}}^{\mathrm{onset}} \approx T_{\mathrm{orb}}^{\mathrm{onset}} = T_{\mathrm{M}}$. In H1, we find $T_{\mathrm{orb}}^{\mathrm{onset}} \gg T_{\mathrm{spin}}^{\mathrm{onset}}$, as discussed in Ref. [7]. The data for the static susceptibilities shown in panels (a)–(d) are adapted from Ref. [7]. A Curie-Weiss analysis of the data of panel (c) is presented in Appendix B.

$\omega_{e1} = +0.5$) into the QP peak in H1 [cf. Fig. 2(i)]. Due to the special SOS screening process, the spin screening only sets in once orbital screening has been completed $T_{\mathrm{orb}}^{\mathrm{cmp}}$, thus $T_{\mathrm{spin}}^{\mathrm{onset}} \approx T_{\mathrm{orb}}^{\mathrm{cmp}}$. As the temperature is lowered into the regime $T_{\mathrm{FL}} < T < T_{\mathrm{spin}}^{\mathrm{onset}}$ also the spins get gradually screened, eventually resulting in the full screening of both spin and orbital degrees of freedom and thus in a FL below T_{FL}. The spin screening is signaled by the formation of a step-like feature in ARPES spectra and by a Pauli-like orbital susceptibility.

This screening route is also reflected in $Z(T)$ [cf. dotted yellow curve in Figs. 7(a) and 7(b)]. For $T_{\mathrm{spin}}^{\mathrm{onset}} < T < T_{\mathrm{orb}}^{\mathrm{onset}}$, the existence of resilient HQPs leads to a plateau-like feature in $Z(T)$. As the temperature decreases into the regime $T_{\mathrm{FL}} < T < T_{\mathrm{spin}}^{\mathrm{onset}}$, $Z(T)$ decreases and approaches a second plateau in the FL regime $T < T_{\mathrm{FL}}$. The reduction of $Z(T)$ shows that the HQPs are additionally "dressed" through spin screening, resulting in heavier Landau QPs.

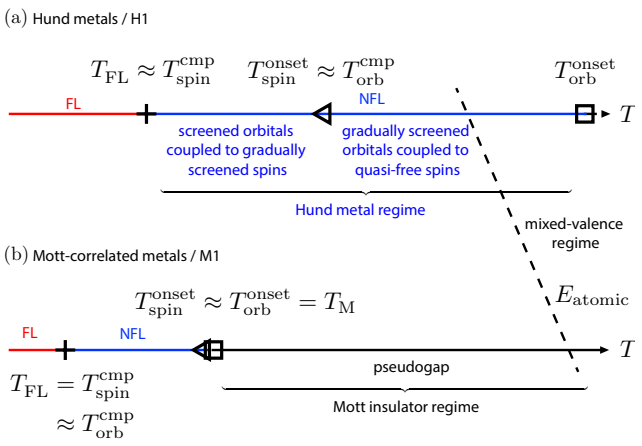

FIG. 8. (a) Schematic sketch of different temperature regimes in a Hund metal. For $T > T_{\rm FL}$, H1 is a NFL up to temperatures in the order of bare energy scales, where also mixed-valence physics becomes important. The NFL regime, which we dub Hund metal regime, reflects the complex SOS screening process of Fig. 3. First orbitals get screened with decreasing temperature for $T^{\rm cmp}_{\rm orb} < T < T^{\rm onset}_{\rm orb}$. In this regime transport is governed by HQPs, which are characterized by gradually screened orbitals coupled to quasi-free spins. Only when the orbital screening process is completed spins get screened below $T^{\rm onset}_{\rm spin} \approx T^{\rm cmp}_{\rm orb}$, i.e., in this regime, the HQPs get gradually dressed to form heavier Landau QPs. For $T < T_{\rm FL} = T^{\rm cmp}_{\rm spin}$, H1 is a FL and both orbital and spin degrees of freedom are fully screened. (b) Schematic sketch of different temperature regimes in a multiorbital Mott-correlated metal. In a Mott system, a pseudogap governs the physics in an extended temperature regime, $T > T^{\rm onset}_{\rm spin} \approx T^{\rm onset}_{\rm orb} = T_{\rm M}$. For temperatures below $T_{\rm M}$, both orbital and spin degrees of freedom get screened simultaneously with the onset of a Kondo resonance, which is driven by the DMFT self-consistency condition. The NFL regime for $T_{\rm FL} < T < T_{\rm M}$ is followed by a low-temperature FL regime, $T < T_{\rm FL} < T^{\rm cmp}_{\rm spin} \approx T^{\rm cmp}_{\rm orb}$, where both orbital and spin degrees of freedom are fully screened.

B. Mott system M1

The Mott system M1 behaves very differently. As shown in Ref. [7], $T_{\rm M} \equiv T^{\rm onset}_{\rm orb} \approx T^{\rm onset}_{\rm spin}$ [cf. black triangle and square in Figs. 7(a) and 7(b)]. For $T > T_{\rm M} \approx 0.15$, both $T\chi_0^{\rm orb}$ and $T\chi_0^{\rm spin}$ exhibit a Curie plateau and the spectral function is characterized by a pseudogap. Both spin and orbital degrees of freedom get screened simultaneously with the onset of a Kondo resonance [cf. Figs. 4(g) and 4(i)], which is driven by the DMFT self-consistency condition, in contrast to the Kondo screening in H1. Interestingly, $T^{\rm onset}_{\rm spin}$ now corresponds to the position of a maximum in $\chi_0^{\rm orb}$ [cf. black triangle and black dashed curve in Figs. 7(c) and 7(d)]: the orbital dynamics is strongly influenced by the spin screening and true Pauli behavior is only reached for $T < T_{\rm FL}$ in M1, thus $T_{\rm FL} = T^{\rm cmp}_{\rm spin} \approx T^{\rm cmp}_{\rm orb}$ for Mott systems.

The behavor described above is summarized in Fig. 8(b). In M1, Mott physics dominates and with increasing temperature essentially destroys SOS physics by opening a pseudogap already at low temperatures. Again, $Z(T)$ reflects these findings [cf. dotted black curve in Figs. 7(a) and 7(b)]. Similar to H1, $Z(T)$ is small and constant for $T < T_{\rm FL}$. But instead of a second HQP plateau as in H1, $Z(T)$ has a maximum directly below $T_{\rm M}$ and diverges for $T > T_{\rm M}$.

C. Intermediate system I2

To corroborate our picture above, we similarly study I2 and W0 in Figs. 7(e)–7(h). I2 is rather close to the Mott boundary [cf. diamond in Fig. 1(a)]. Thus, we observe Mott signatures at high temperatures: for $T > T_{\rm M} \equiv T^{\rm onset}_{\rm orb} \approx 0.25$, $T\chi_0^{\rm orb}$ shows Curie behavior [cf. red square in Figs. 7(e) and 7(f)] and a pseudogap exists [cf. Figs. 5(g) and 5(i)]. However, due to the large $J = 2$, we find Hund signatures, as well, at intermediate and low temperatures: orbital and spin screening are slightly separated, $T^{\rm onset}_{\rm orb} > T^{\rm onset}_{\rm spin}$, and $Z(T)$ features a plateau for $T^{\rm onset}_{\rm spin} < T < T^{\rm onset}_{\rm orb}$ (between red triangle and square). $T^{\rm onset}_{\rm spin}$ marks a maximum in $\chi_0^{\rm orb}$ [cf. Figs. 7(g) and 7(h)], which is however less pronounced than for M1. Full screening with Pauli behavior of both $\chi_0^{\rm orb}$ and $\chi_0^{\rm spin}$ is reached at $T < T_{\rm FL}$. Due to the large Hund's coupling, $T_{\rm FL}$ (and accordingly $Z(T = 0)$ [35]) is lowest in I2 compared to H1, M1, and W0. In sum, I2 exhibits an intermediate system, showing a mixture of Hund and Mott features.

D. Weakly correlated system W0

Finally, we consider the weakly correlated system W0, a system without Hund's coupling, $J = 0$ (cf. also Fig. 6). In Figs. 7(e)–7(h), $\chi_0^{\rm orb}$ and $\chi_0^{\rm spin}$ behave similarly for W0, up to a constant prefactor: $\chi_0^{\rm spin}/\chi_0^{\rm orb} = 1.5$. The FL regime extends up to very high temperatures [$Z(T)$ is essentially constant in an extended regime in Figs. 7(e) and 7(f)]. Both Hund and Mott features are absent in W0.

VI. TRANSPORT PROPERTIES AND ENTROPY

In this section we add further perspective to the differences and similarities of the four systems H1, M1, I2, and W0 by discussing the temperature dependence of various transport properties and the entropy. For completeness, Appendix D collects some elementary definitions and relations involving the quantities discussed below.

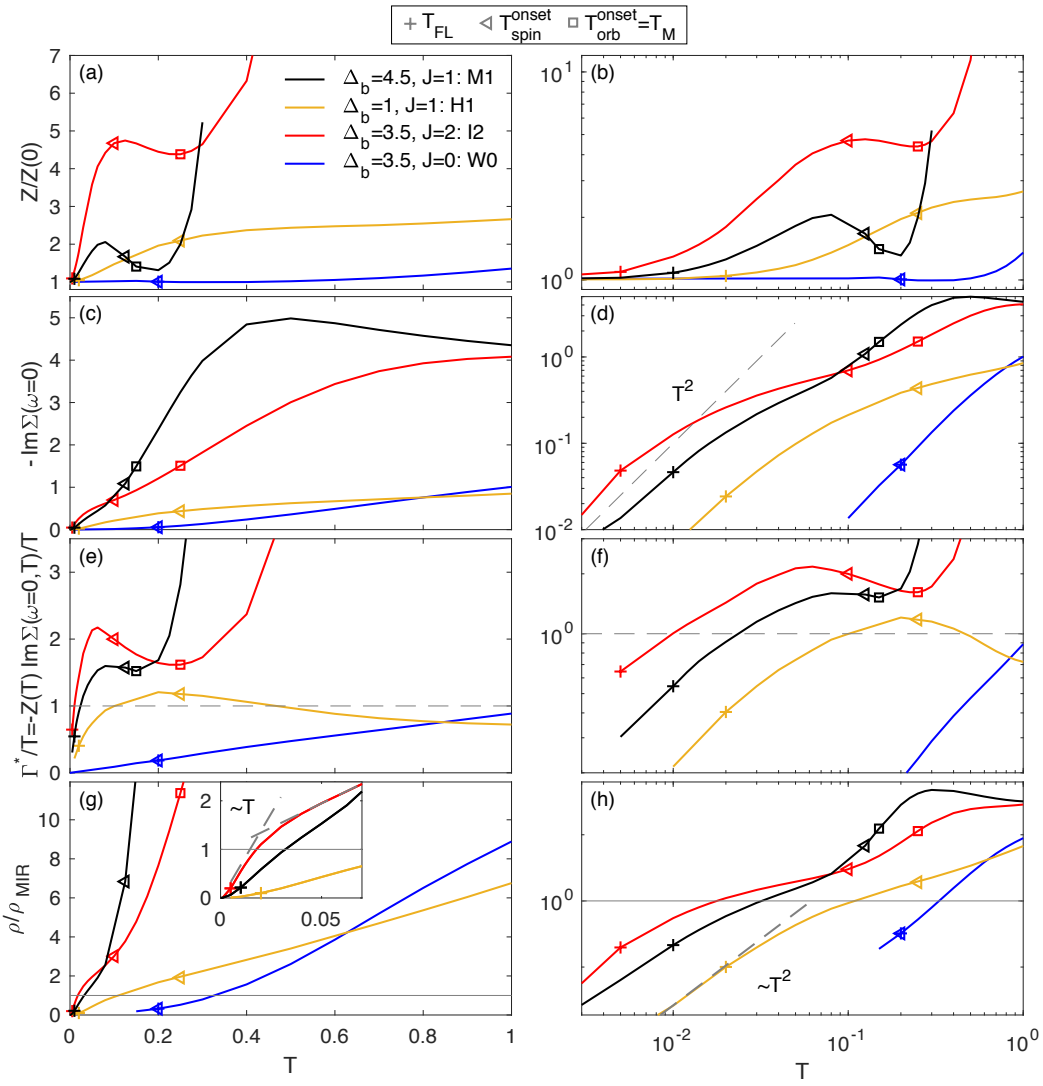

FIG. 9. [(a),(b)] The quasiparticle weight $Z/Z(0)$ (replotted from Fig. 7 for reference), [(c),(d)] the scattering rate at the Fermi level $\mathrm{Im}\,\Sigma(\omega=0)$, [(e),(f)] the coherence scale Γ^*/T, and [(g),(h)] the resistivity ρ, all plotted as functions of temperature on a linear (left) and a logarithmic (right) scale for M1 (black), H1 (yellow), I2 (red), and W0 (blue). Symbols are defined as in Fig. 7. [(d),(h)] The dashed grey guide-to-the-eye lines indicate FL behavior. [(e),(f)] The horizontal dashed grey lines mark $\Gamma^*/T^*=1$. [(g),(h)] The horizontal solid grey line marks the MRI limit defined via $k_\mathrm{F} l_\mathrm{min} \approx 2\pi$.

A. Scattering rate at the Fermi level

Figure 9 shows the temperature dependence of the quasiparticle weight, the scattering rate, the coherence scale, and the resistivity. We now discuss them in turn.

The scattering rate $-\mathrm{Im}\,\Sigma(\omega=0)$ is plotted as a function of temperature in Figs. 9(c) and 9(d). For $T<T_\mathrm{FL}$, $-\mathrm{Im}\,\Sigma(\omega=0)$ follows FL behavior [cf. dashed grey guide-to-the-eye line in Fig. 9(d)]. In H1, for $T>T_\mathrm{FL}$, the scattering rate is small and shows a crossover to a rather flat behavior in the HQP regime. By contrast, in M1, the scattering rate increases strongly [cf. Fig. 9(e)], saturating at high temperatures due to the presence of a pseudogap. I2 shows a mixture of both the Hund and the Mott behavior. $-\mathrm{Im}\,\Sigma(\omega=0)$ first flattens somewhat for $T_\mathrm{FL}<T<T_\mathrm{spin}^\mathrm{onset}$, but then increases strongly for $T>T_\mathrm{spin}^\mathrm{onset}$, saturating as well at very high temperatures. Notably, $-\mathrm{Im}\,\Sigma(\omega=0)$ is larger for I2 than for M1 for $T<0.1$; this is caused by the larger $J=2$ in I2. The scattering rate in W0 is small and FL-like. It keeps growing slowly with increasing temperature.

B. Coherence scale

In Figs. 9(e) and 9(f) we plot Γ^*/T, with the inverse QP lifetime, defined as

$$\Gamma^*(T) = -Z(T)\mathrm{Im}\,\Sigma(\omega=0,T)\,. \qquad (6)$$

In a FL, i.e., for $T \lesssim T_{\mathrm{FL}}$, one expects $\Gamma^*(T) \propto T^2$. The coherence scale T^* is defined as $\Gamma^*/T^* \equiv 1$ (cf. intercepts with horizontal dashed grey line). Above T^* coherent Landau QPs become short-lived and the FL picture breaks down.

H1 is characterized by a very broad maximum of Γ^*/T in the NFL regime around $T_{\mathrm{spin}}^{\mathrm{onset}}$. This behavior is reminiscent of DFT+DMFT results for Sr_2RuO_4, where Γ^*/T keeps increasing in a FL-to-NFL crossover regime above $T^* \approx 100\,\mathrm{K}$ and finally reaches a plateau above 350 K [22]. By contrast, M1 shows only a narrow plateau in Γ^*/T around $T_{\mathrm{spin}}^{\mathrm{onset}}$ before it diverges [due to the divergence of $Z(T)$]. Again, I2 features a mixture of both the Hund and the Mott behavior. Γ^*/T first exhibits a maximum at $T_{\mathrm{spin}}^{\mathrm{onset}}$, but then diverges above $T_{\mathrm{orb}}^{\mathrm{onset}}$. In W0, Γ^*/T is very small and grows linearly with increasing temperature, implying $\Gamma^* \propto T^2$.

C. Resistivity

The resistivity $\rho(T)$ is shown in Figs. 9(g) and 9(h). In the FL regime, we find T^2 behavior (though this is hard to resolve very accurately). Equivalently to the findings for a hole-doped Mott insulator [76], we observe for H1 and I2 that in the regime $T_{\mathrm{FL}} < T < T_{\mathrm{spin}}^{\mathrm{onset}}$, $\rho(T)$ first increases approximately linearly with a negative intercept, then it shows a slope-decreasing knee-like feature, above which a linear increase with positive intercept sets in. The inset of Fig. 9(g) highlights this for I2 using grey dashed lines, which approximate the behavior of the red curve. For H1 (yellow curve), $\rho(T)$ keeps increasing linearly up to the highest temperature plotted, and thus behaves qualitatively in the same way as the hole-doped Mott insulator of Ref. [76]. This is an intriguing similarity, considering that both systems are assumed to be governed by resilient QPs in their NFL regime. Moreover, our findings for H1 are reminiscent of the DFT+DMFT simulations [9] and measurements [66] of the resistivity in iron pnictides. In contrast to H1, for I2 a second (slope-increasing) knee occurs at $T_{\mathrm{spin}}^{\mathrm{onset}}$, beyond which $\rho(T)$ grows rapidly with increasing temperature until it saturates above $T_{\mathrm{orb}}^{\mathrm{onset}}$ in the presence of a stable pseudogap. For M1 (black curve), we do not observe a slope-decreasing knee, but instead a slope-increasing knee at $T \approx 0.08$, above which $\rho(T)$ increases rapidly with growing temperature [cf. Fig. 9(h)]. W0 is again characterized by a large FL regime, reaching up to very high temperatures. For all but the largest temperatures, $\rho(T)$ is much smaller for the system with $J = 0$ than for those with finite J. (At very high T, the resistivity $\rho(T)$ of W0 increases past that of H1; the reason is that the scattering rate $-\mathrm{Im}\Sigma(\omega = 0, T)$ of W0 likewise increases past that of H1 [cf. Figs. 9(c) and 9(d)], reflecting the fact that the former has a larger bare gap, $\Delta_b^{\mathrm{W0}} = 3.5$ vs $\Delta_b^{\mathrm{H1}} = 1$.) We remark that for all systems $\rho(T)$ crosses the Mott-Ioffe-Regel (MIR) limit, ρ_{MIR} [cf. horizontal solid grey line in Figs. 9(g) and 9(h) and Appendix D 1 for a definition of ρ_{MIR}] and continues to grow above this limit. As expected, M1 crosses the MIR limit at a smaller temperature scale than H1. Notably, I2 crosses the MIR limit at an even lower scale although Coulomb interactions are larger in M1 than in I2. This strong correlation effect is due to Hundness, i.e., large J.

To conclude this subsection, we remark that an analysis of the temperature dependence of the optical conductivity $\sigma(\omega)$ for I2 is presented in Appendix C.

D. Effective chemical potential of quasiparticles

We now turn to Fig. 10. We first study the evolution of the effective chemical potential for QPs, $\mu_{\mathrm{eff}} = \mu - \mathrm{Re}\,\Sigma(\omega = 0)$, in Figs. 10(a) and 10(b). For $T < T_{\mathrm{FL}}$, μ_{eff} is constant, i.e., Luttinger pinning holds (cf. Sec. 3.10.2 of Ref. [73] for details). Interestingly, for the finite-J systems μ_{eff} increases towards 0 with increasing temperature, $T_{\mathrm{FL}} < T < T_{\mathrm{spin}}^{\mathrm{onset}}$, i.e., towards an effective half-filling of the system. In H1, this trend is retained above $T_{\mathrm{spin}}^{\mathrm{onset}}$ until μ_{eff} approaches a plateau in the mixed-valence regime. This behavior fits to the SOS screening picture (cf. Figs. 3 and 8) where, above T_{FL}, spins are gradually unscreened to form an effective 3/2 spin (which implies effective half filling), while the orbitals are still in an orbital singlet for $T < T_{\mathrm{spin}}^{\mathrm{onset}}$. For $T > T_{\mathrm{spin}}^{\mathrm{onset}}$, the orbitals start to get unscreened while large quasi-free spins persist. In M1, μ_{eff} drastically reduces for $T > T_{\mathrm{M}}$, reflecting the formation of a pseudogap. In I2, μ_{eff} first increases markedly almost up to 0 and then decreases for $T > T_{\mathrm{orb}}^{\mathrm{onset}}$, similarly to M1. By contrast, for $J = 0$, W0 directly decreases above T_{FL}. The substantial continuous increase of $\mu_{\mathrm{eff}}(T)$ with increasing temperature towards half-filling, i.e., an inflating Fermi volume, is clearly connected to the existence of a finite J in the 3HHM, while the decrease of $\mu_{\mathrm{eff}}(T)$ with increasing temperature is a Mott feature.

E. Thermopower

In Figs. 10(c) and 10(d) we show the thermopower (Seebeck coefficient) $\alpha(T)$ [as defined in Eq. (D5)] and compare the 3HHM results to the thermopower of Sr_2RuO_4 reported in Ref. [42]. In the FL regime, the thermopower of the 3HHM at $n_d = 2$ shows an electron-like decrease, i.e., $\alpha(T) < 0$. This is qualitatively consistent (modulo a particle-hole transformation) with the hole-like increase, $\alpha(T) > 0$, observed for Sr_2RuO_4, which in a 3HHM-type description would correspond to $n_d = 4$. However, our data is not accurate and dense enough to unveil FL behavior, $\alpha(T) \propto T$. Similar to the (broad) maximum in $\alpha(T)$ of Sr_2RuO_4 around 300 – 500 K, we observe a minimum in the crossover regime $T_{\mathrm{FL}} < T < T_{\mathrm{spin}}^{\mathrm{onset}}$. In H1, we further find a saturation (broad maximum) well above $T_{\mathrm{spin}}^{\mathrm{onset}}$. In I2 and M1, a

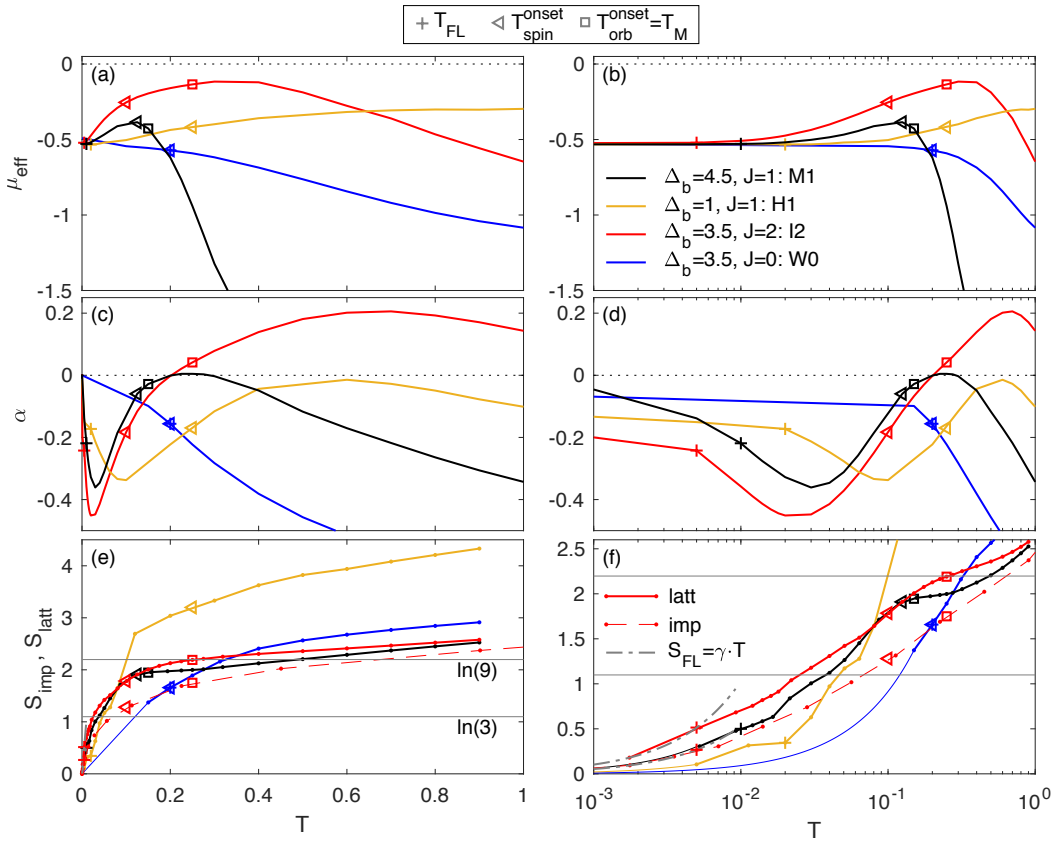

FIG. 10. [(a),(b)] The effective chemical potential $\mu_{\rm eff}$, [(c),(d)] the thermopower α, and [(e),(f)] the lattice entropy $S_{\rm latt}$ (solid) and the impurity contribution to the entropy $S_{\rm imp}$ (dashed), all plotted as functions of temperature on a linear (left) and logarithmic (right) scale for M1 (black), H1 (yellow), I2 (red), and W0 (blue). Symbols are defined as in Fig. 7. In (f), the grey dash-dotted curves indicate FL behavior for $S_{\rm imp}$ and $S_{\rm latt}$, respectively. We remark that wiggles in $S_{\rm latt}$ are an artefact due to few data points used in its computation.

maximum occurs above $T_{\rm orb}^{\rm onset}$, as well. Overall, the behavior of $\alpha(T)$ is similar for all systems with finite J. However, the minimum is much more extended and lies at higher energies in H1 compared to M1 [cf. Fig. 10(c)]. In contrast, W0 with $J = 0$ does not exhibit any minimum (or maximum) in $\alpha(T)$. Here, the thermopower decreases in a FL-like fashion in an extended temperature range.

In sum, we conclude that H1 reflects the findings of Ref. [42]. Using $t \approx 5000$ K (a value which is estimated from a comparison of the model bandwidth with the realistic bandwidth of Sr_2RuO_4 [7]), the minimum of $\alpha(T)$ of H1 is indeed in the same temperature range (300 – 500 K) as the maximum observed for Sr_2RuO_4. Our results support the suggestion made in Ref. [42] that this unusual feature in $\alpha(T)$ can be associated with quenched orbitals and fluctuating spins as present in the two-stage SOS screening process. To be more precise, the minimum of $\alpha(T)$ in the 3HHM corresponds to the crossover regime, where the spins get gradually screened to form coherent Landau QPs. Thus, this minimum in $\alpha(T)$ is observed together with the formation of the step-like ARPES feature [cf. Fig. 2(d)].

F. Entropy

We conclude our study of Hund and Mott features in the 3HHM by calculating the lattice entropy for H1, M1, I2, and W0. For I2, we additionally calculate the impurity contribution to the entropy [cf. Fig. 10(e) and 10(f)]. We start our discussion with I2. For the computation of the lattice entropy $S_{\rm latt}(T)$, we use Eq. (D8). The impurity contribution to the entropy $S_{\rm imp}(T)$ is obtained with Eq. (D7). Remarkably, we find that $S_{\rm latt}(T)$ is larger than $S_{\rm imp}(T)$ in the whole temperature range $0 < T < 1$, while both entropies behave qualitatively in the same way. The difference between $S_{\rm latt}(T)$ and $S_{\rm imp}(T)$ already arises in the FL regime, where the entropy is given as

$$S(T) = \gamma T \tag{7a}$$

$$\gamma = \frac{2N_c\pi^2}{3\mathcal{Z}}. \tag{7b}$$

When computing the lattice or impurity entropies, $S_{\rm latt}$ or $S_{\rm imp}$, the parameter $\mathcal{Z}$ should be equated to the mass renormalizations, $Z_{\rm latt}$ or $Z_{\rm imp}$, derived from the lattice

or impurity Green's functions, respectively. The former is given by $Z_{\rm latt} = [1 - \partial_\omega {\rm Re}\,\Sigma(\omega)|_{\omega=0}]^{-1}$. The latter, found by a first-order expansion of $G_{\rm imp}(\omega) = [\omega - \varepsilon_d - \Delta(\omega) - \Sigma(\omega)]^{-1}$, where $\Delta(\omega)$ is the self-consistent hybridization function, is given by $Z_{\rm imp} = [Z_{\rm latt}^{-1} - \partial_\omega {\rm Re}\,\Delta(\omega)|_{\omega=0}]^{-1}$ (cf. Sec. 3.9 in Ref. [73] for details). Obviously, DMFT generically yields $Z_{\rm latt} < Z_{\rm imp}$ in the FL regime (when using a Bethe lattice). This implies that $S_{\rm latt} > S_{\rm imp}$, as found numerically above. Although this insight can be simply derived, we are not aware of any previous results that explicitly demonstrated this quantitative difference of the impurity and the lattice entropy. Its implication is that $S_{\rm imp}$ can not be regarded as a quantitatively reliable proxy for $S_{\rm latt}$.

Nevertheless both entropies for I2 reveal the two-stage SOS screening process. For $T > T_{\rm orb}^{\rm onset}$, I2 is characterized by a pseudogap and both the spin and orbital degrees of freedom are unscreened, resulting in $S_{\rm latt} > \ln(9)$. [$S_{\rm latt}$ slightly exceeds $\ln(9)$ because of remaining active charge fluctuations in the pseudogap regime.] $S_{\rm imp}$ crosses $\ln(9)$ at slightly higher temperatures. For $T < T_{\rm orb}^{\rm onset}$, $S_{\rm latt}(T)$ and $S_{\rm imp}(T)$ decrease continuously with decreasing temperature, reflecting the screening of orbital degrees of freedom, while spin degrees of freedom are still quasi-free. We observe that $S_{\rm latt}(T)$ crosses $\ln(3)$ below $T_{\rm spin}^{\rm onset}$, while $S_{\rm imp}(T)$ crosses $\ln(3)$ at about $T_{\rm spin}^{\rm onset}$. The value $\ln(3)$ is associated with a spin triplet and an orbital singlet. For $T < T_{\rm FL}$ we find FL behavior for both $S_{\rm latt}$ and $S_{\rm imp}$, indicated by the dash-dotted grey fits, respectively [cf. Fig. 2(f)].

Overall, we clearly observe that the two-stage SOS screening process is a continuous process: the entropy continuously decreases with decreasing temperature, i.e., no stable NFL fixed point is reached in the system (this was already pointed out in the Supplemental Material of Ref. [33]). Instead, we are faced with an intriguingly complex crossover behavior.

The two-stage SOS screening process is also manifest in $S_{\rm latt}$ for H1 and M1. While the qualitative behavior is similar, quantitative details differ. In the FL regime, $S_{\rm latt}$ is smaller for H1 than for M1, since $S_{\rm latt} \propto T/Z_{\rm latt}$ (and H1, having smaller U, has less mass enhancement, i.e., larger $Z_{\rm latt}$). Above $T_{\rm FL}$, $S_{\rm latt}$ increases strongly for H1, leading to a very large entropy ($> \ln(9)$) above $T_{\rm spin}^{\rm onset}$. We interprete this as a consequence of large charge fluctuations due to small Coulomb interactions. By contrast, $S_{\rm latt}$ for M1 approaches $\ln(9)$ above $T_{\rm M}$ and only slightly exceeds $\ln(9)$ for very high temperatures.

Very recently, a detailed study of the temperature dependence of the entropy and specific heat of a three-band Hubbard model has been performed [80]. This study is much more comprehensive than ours. Their results are not directly comparable to ours, although, since their interaction term contained only density-density terms but no spin-flip terms.

VII. CONCLUSION

A. Fingerprints of Hund versus Mott physics

In this paper we have used DMFT+NRG to investigate the normal state properties of the degenerate three-band Hubbard-Hund model (3HHM) with focus on 1/3 filling, a minimal model with relevance for Hund metals. Our paper has been based on the following key question: What are the decisive fingerprints of a Hund metal as opposed to a Mott-correlated metal? We conclude by giving a summary-style overview of the fingerprints found in the present paper.

At $T = 0$, finite J induces an intertwined two-stage SOS Kondo-type screening process in the 3HHM at $n_d = 2$, in which orbital and spin degrees of freedom are explicitly coupled: below $T_{\rm orb}$, the orbital degrees of freedom form an orbital singlet through the formation of a large effective Hund's-coupling-induced impurity spin of 3/2—*including* a bath spin degree of freedom; and below $T_{\rm spin}$, the spin-3/2 is fully screened by the three bath channels of the 3HHM. In the frequency domain this screening process results in three characteristic regimes: a FL regime, a NFL crossover regime, and a NFL HQP regime. At zero temperature, clear signatures of SOS include: (i) a low-frequency FL regime with a narrow "needle"-formed SU(2) Kondo peak in the local density of states, a low-frequency Landau QP band with a small slope given by Z in ARPES spectra, FL scaling of the self-energy, a Drude peak in the optical conductivity (cf. Appendix C); (ii) a NFL crossover regime signaling the deviation from FL behavior characterized by a step-like feature in the dispersion at $\omega < 0$ and a kink at $\omega > 0$ [accordingly, ${\rm Re}\,\Sigma(\omega < 0)$ exhibits a pronounced maximum]; and (iii) an intermediate-frequency NFL "Hund quasiparticle" (HQP) regime with a SU(3) Kondo resonance in the local density of states, also identifiable as excess spectral weight in the optical conductivity (cf. Appendix C) and as a resilient slightly particle-hole asymmetric steep "HQP band" in ARPES spectra (waterfall structure), which is extended over a large frequency range, where the scattering rate is only weakly energy dependent [e.g., there is a shoulder in ${\rm Im}\,\Sigma(\omega < 0)$]. We remark that the particle-hole asymmetry of the 3HHM leads to two distinct FL scales in the frequency domain and to very different features in the SOS window at negative and positive frequencies (e.g., in ARPES spectra). These SOS features (cf. Fig. 11 for an overview) are generic and are found for both the metallic H1 and the metallic M1, since SOS physics is essentially impurity physics [33]. However, there is an important difference.

A Hund metal, such as H1, lies far from any MIT phase boundary. Strong correlations are primarily induced by the two stage SOS Kondo-type screening, which leads to the localization of spins rather than charges. The incoherent SOS window is extended over a broad range of energies, reaching up to bare excitation scales. In the 3HHM, at high frequencies, the SU(3) Kondo resonance

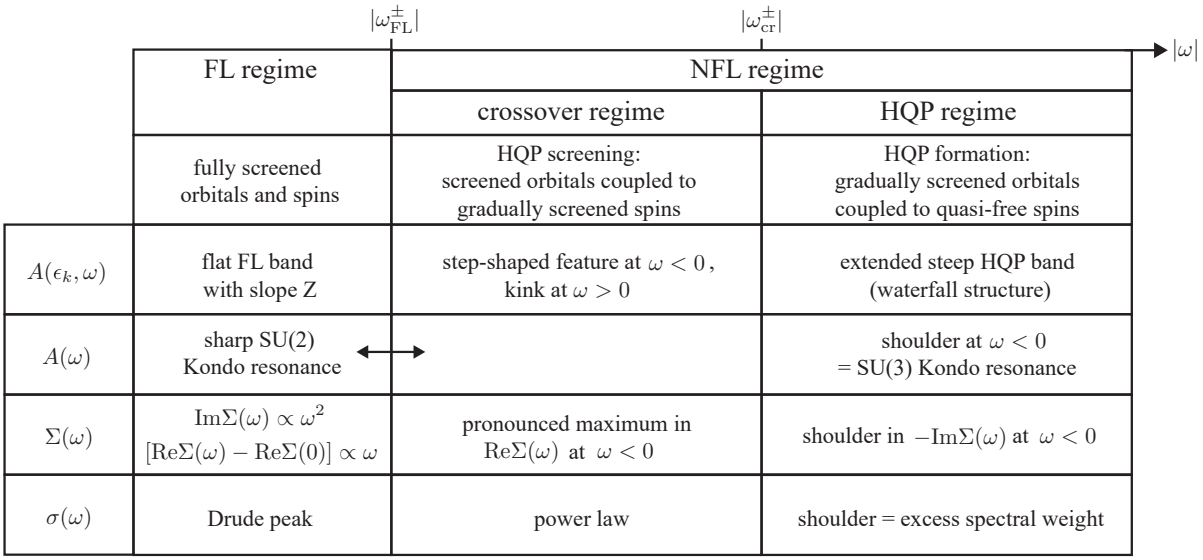

FIG. 11. Overview of important SOS features in the 3HHM for $n_d = 2$ at $T = 0$. Features are described as functions of decreasing frequency.

(shoulder) merges with the Hubbard bands. At very low temperatures, the local density of states exhibits a two-tier quasiparticle peak on top of a broad incoherent background.

By contrast, Mott-correlated metals with $\sim 1/3$ filling such as V_2O_3 [7], represented in our study by M1, are close to the MIT phase boundary. Thus, at zero temperature, both $T_{\rm orb}$ and $T_{\rm spin}$ are strongly reduced compared to bare excitation scales and the SOS window is very small, i.e., a narrow QP peak exists between well-separated pronounced Hubbard bands.

In Hund metals, the SOS screening process also governs the temperature dependence of Hund metals, up to highest temperatures. Most importantly, we argue that the nature of the incoherent transport regime is governed by resilient HQPs, while the FL regime is described in terms of Landau QPs. In Ref. [7], we have identified two different temperature scales for the onset of orbital and spin screening in Hund metals, $T^{\rm onset}_{\rm orb}$ and $T^{\rm onset}_{\rm spin}$, respectively. For $T^{\rm onset}_{\rm spin} < T < T^{\rm onset}_{\rm orb}$, HQPs dominate the high-temperature physics and lead to a Curie-like static spin susceptibility (while the static orbital susceptibility is a decreasing function of temperature) and a resilient QP peak (without substructure) in the local density of states. In the 3HHM, we find a robust HQP band in ARPES spectra, an additional HQP plateau in $Z(T)$, a rather flat (electron-like) scattering rate, a linear resistivity exceeding the MIR limit, and an inflated Fermi volume ($\mu_{\rm eff}$ increases with increasing temperature). At very high temperatures, mixed-valence physics additionally comes into play. Due to the special SOS screening process, the spins can only get screened as soon as the orbitals are fully screened at $T^{\rm cmp}_{\rm orb}$, thus $T^{\rm onset}_{\rm spin} \approx T^{\rm cmp}_{\rm orb}$. For $T_{\rm FL} < T < T^{\rm onset}_{\rm spin}$ also the spins are gradually screened, eventually resulting in the full screening of both degrees of freedom and thus in a FL below $T_{\rm FL} = T^{\rm cmp}_{\rm spin}$. The spin screening is signalled by the formation of a step-like feature in ARPES spectra, while the completion of orbital screening is characterized by a Pauli-like orbital susceptibility. In this regime, the thermopower has a minimum. A corresponding feature in the thermopower is observed in experiments for ruthenates. [42].

By contrast, in Mott-correlated metals, with increasing temperature, SOS features (and HQPs) only survive at very low temperatures, whereas the behavior at higher temperatures is fully governed by classical Mott physics (as known from the one-band Hubbard model): the DMFT self-consistency condition opens up a pseudogap in the local spectrum by localizing the charges. Conversely, with decreasing temperature, spin, and orbital degrees of freedom get screened simultaneously at the temperature scale, $T_{\rm M} = T^{\rm onset}_{\rm orb} \approx T^{\rm onset}_{\rm spin}$, with the onset of a Kondo resonance, driven by DMFT. Only below $T_{\rm FL} = T^{\rm cmp}_{\rm spin} \approx T^{\rm cmp}_{\rm orb}$ both the spin and the orbital degrees of freedom get fully screened.

All important temperature-dependent signatures for H1 and M1 are summarized in Fig. 12.

In sum, we shed light on two qualitatively different screening routes from the atomic degrees of freedom to the emerging heavy QPs in strongly correlated systems, driven by Hundness or Mottness, and corroborated that Hundness, i.e., SOS Kondo-type screening, dominates the anomalous physics of Hund metals in terms of resilient HQPs.

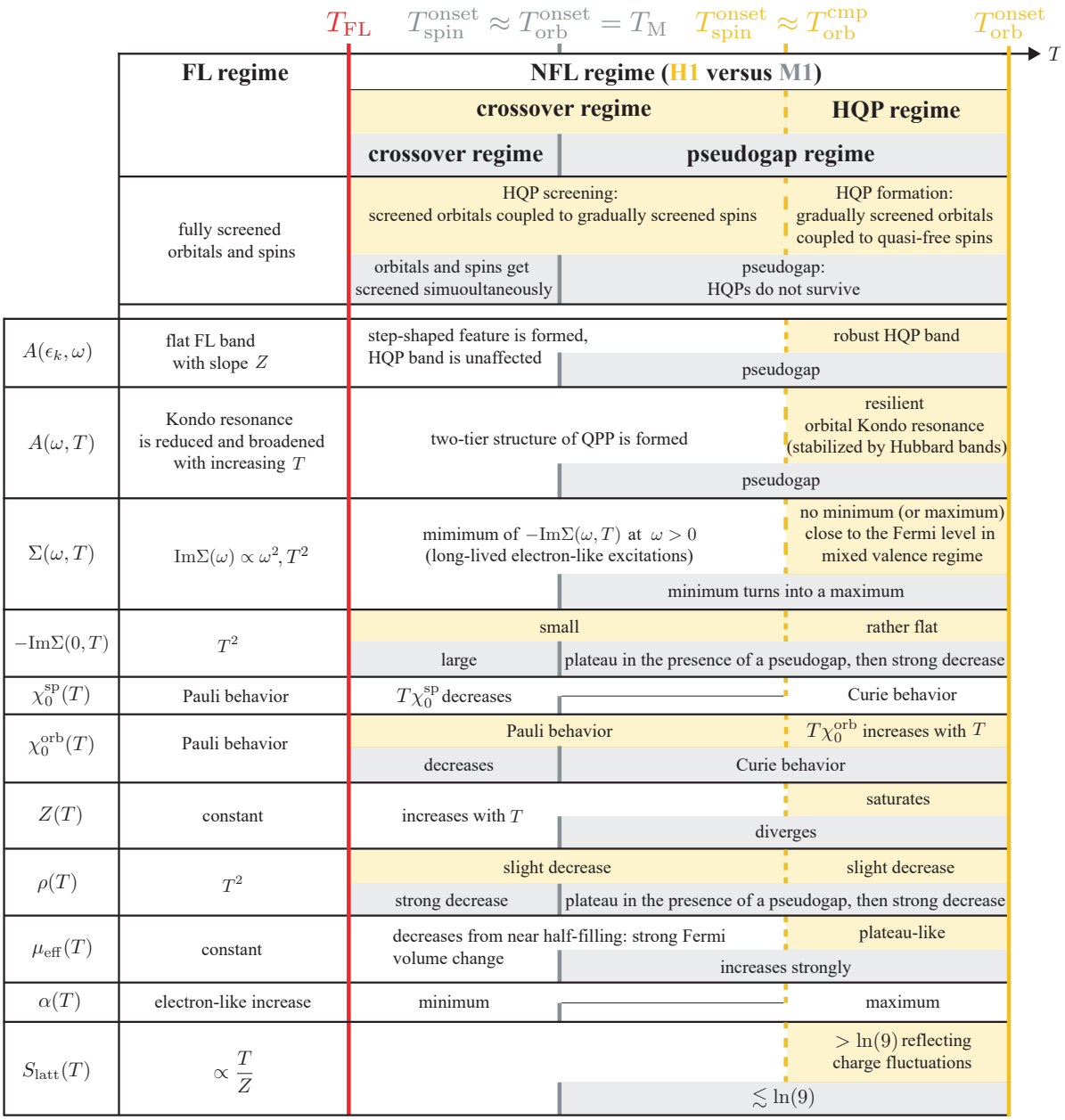

FIG. 12. Overview of important Hund and Mott features in the temperature dependence of various physical quantities. Hund-related features are marked yellow, Mott-related features are marked grey. Common features are on white background. Note that the temperature scale is only schematic. Features are described as functions of decreasing temperature.

B. Physics beyond the minimal three-band Hund-Hubbard model

In the present study we purposefully focused on the 3HHM, the simplest possible Hamiltonian capturing the essence of Hund and Mott physics. We thereby neglected several complications occurring in real materials. Let us now briefly comment on these. First, to fully exploit the power of the NRG, we used a Coulomb interaction matrix with $\mathrm{U}(1)_{\mathrm{ch}}\times\mathrm{SU}(2)_{\mathrm{spin}}\times\mathrm{SU}(3)_{\mathrm{orb}}$ symmetry, avoiding more realistic parametrizations of the Coulomb interaction such as the Kanamori parametrization. Second, we neglected the spin-orbit coupling, which reduces the symmetry to $\mathrm{U}(1)_{\mathrm{ch}}\times\mathrm{SU}(2)_{\mathrm{tot}}$ or even weaker symmetries, where "tot" stands for total angular momentum. The spin-orbit coupling terms have been shown to be irrelevant in the renormalization group sense [81], i.e., they do not affect the system's low-energy behavior unless the coupling strength is larger than T_{orb}. Third, we neglected crystal field splittings. Fourth, we took a very

simple bipartite Bethe lattice, thereby ignoring effects arising from realistic electronic dispersions and Fermi surfaces. Spin-orbit coupling, crystal fields, and realistic band structures all bring about important physical effects not present in our model. These include orbital differentiation and even orbital-selective Mott transitions (see, for example, Refs. [60, 82–85]), where one orbital becomes much more correlated than others or even completely localized. Incorporating such realistic aspects is the focus of intensive current investigations in multiple materials and models (see, for example, Refs. [86–88]). Such studies will benefit from the deeper understanding, achieved in our paper, of the finite-temperature Hund metal state and how it is modified as the Mott transition is approached. In this sense, our paper sets the stage for future studies incorporating additional material-specific physical effects.

Finally, an important aspect that was not studied in our paper is the appearance of symmetry-broken phases in Hund metals at low temperatures, e.g., magnetic [89, 90], insulating [91], and superconducting [41, 74, 92, 93] phases. Generalizations and extensions of the DMFT+NRG approach used here could be developed to achieve a deeper understanding of these phases, and how they emerge from the Hund metal state.

In the long run, such studies would also have to include the effects of nonlocal correlations and nonlocal interactions, neglected here, e.g., by using nonlocal extensions of DMFT [94–104]. Nonlocal correlations are generally expected to be weaker in Hund metals than Mott systems [105]. We also expect nonlocal interactions to be less important as the screening of the nonlocal interactions is more efficient in metallic systems. Nevertheless, clarifying how nonlocal correlations and nonlocal interactions affect the physics of Hund metals is a very interesting question which is only beginning to be studied [106].

C. Experimental signatures of two-stage screening

Although our minimal 3HHM neglects numerous effects relevant for realistic materials, as discussed above, the physics, which it does capture, in particular two-stage screening and SOS, is expected to be robust. Indeed, indications of two-stage screening of electrons have been found in several experimental studies. For example, they were identified in various members of the iron pnictides and chalcogendies by means of infrared spectroscopy [68, 107]; resistivity, heat-capacity, thermal-expansion, susceptibility measurements [66, 67]; quasiparticle scattering interference [14]; proximity effect [50]; and ARPES [108, 109]. A second prototypical system of a Hund metal is Sr_2RuO_4, where optical conductivity [77], thermopower [42], and ARPES [78] provide multiple signatures of Hund metal behavior. We hope that the present paper of a minimal three-band model, containing the minimal ingredients to yield Hund and/or Mott physics, will assist future experimental studies in attributing observed features to either Hund rule effects (Hundness) or charge-blocking effects (Mottness).

ACKNOWLEDGMENTS

We thank F. B. Kugler for helpful discussions. K.M.S., S.-S.B.L., and J.v.D. were supported by the Deutsche Forschungsgemeinschaft (DFG, German Research Foundation) under Germany's Excellence Strategy EXC-4 (Project No. 24040814) and EXC-2111 (Project No. 390814868) and through Project No. 409562408. S.-S.B.L. acknowledges the DFG grant LE3883/2-1 (Project No. 403832751). A.W. was supported by the U.S. Department of Energy, Office of Science, Basic Energy Sciences, Materials Sciences and Engineering Division under Contract No. DE-SC0012704. G.K. was supported by NSF grant DMR-1733071.

Appendix A: Asymmetry of frequency-dependent quantities at zero temperature

In this Appendix, we investigate in more detail the particle-hole asymmetry of the 3HHM at zero temperature discussed in the main text. In particular, we look at the frequency-dependence of the self-energy, the local spectral function, the dynamical spin and orbital susceptibilities, the optical conductivity, and the kinetic energy.

A first detailed temperature-dependent study of the implications of particle-hole asymmetry in Hubbard-type models was given in Ref. [76] for a one-band hole-doped Mott insulator, i.e., for a model with only one type of degrees of freedom (spins). It was shown that a well-defined QP peak of "resilient" QP excitations exists above the FL scale T_{FL} and that it dominates an intermediate incoherent transport regime up to T_{MIR}. Above this temperature the resistivity exceeds the MIR limit (cf. Appendix D 1 for a definition) and the resilient QPs eventually disappear, or more specifically, the QP peak merges with the lower Hubbard band. Interestingly, the resilient QPs are longer-lived for electron-like than for hole-like excitations, due to the particle-hole asymmetry in the model. This asymmetry further leads to different scales, ω_{FL}^{-} and ω_{FL}^{+}, below which FL behavior is found at negative and positive frequencies at $T = 0$.

In Fig. 13 we revisit the self-energy $\Sigma(\omega)$, the spectral function $A(\omega)$, and the orbital and spin susceptibilities, $\chi_{\mathrm{orb}}(\omega)$ and $\chi_{\mathrm{spin}}(\omega)$ [Eqs. (5)], at $T = 0$. We consider system I2 ($\Delta_b = U - 2J = 3.5$, $J = 2$) which features a broad SOS window, well separated from the Hubbard side bands. We start with a detailed investigation of the FL regime (cf. left panels of Fig. 13) and then concentrate on the SOS window (cf. right panels of Fig. 13). Due to the universal behavior of the model with respect to Δ_b (respectively U) (cf. Fig. 10 of Ref. [35]) the following findings are generic in the metallic regime of the 3HHM,

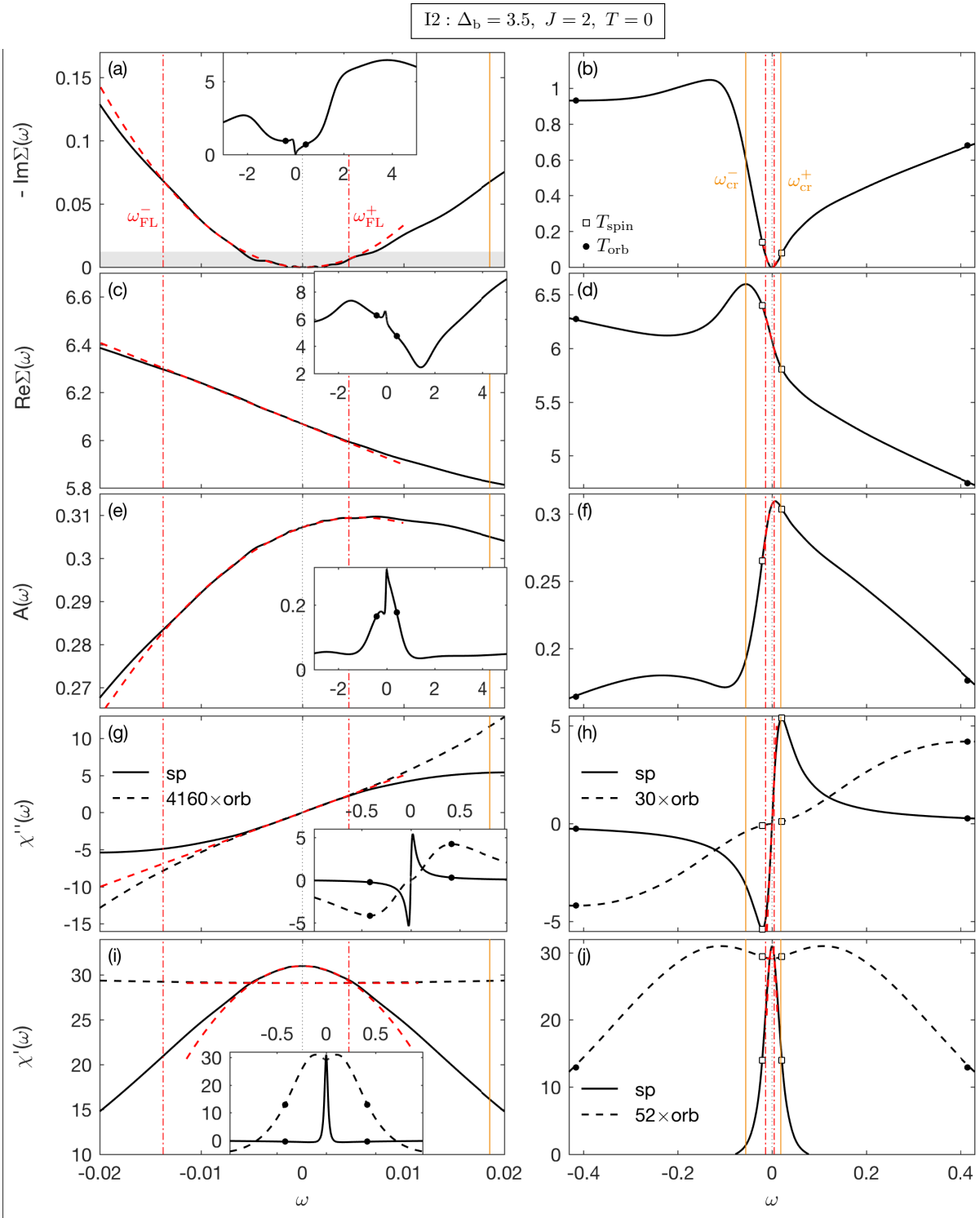

FIG. 13. [(a),(b)] The imaginary part $\mathrm{Im}\,\Sigma(\omega)$ and [(c),(d)] the real part $\mathrm{Re}\,\Sigma(\omega)$ of the self-energy; [(e),(f)] the local spectral function $A(\omega)$; [(g),(h)] the imaginary part $\chi''(\omega)$ and [(i),(j)] the real part $\chi'(\omega)$ of the spin (solid) and orbital (dashed) susceptibilities are plotted versus frequency for I2 ($\Delta_b = 3.5$, $J = 2$) at $T = 0$. Left panels are zooms into the FL regime, whereas their insets show the quantities on a large frequency range. The SOS window is presented in the right panels. Dashed red fits reveal FL behavior for $\mathrm{Im}\,\Sigma(\omega)$, $\mathrm{Re}\,\Sigma(\omega)$, and $A(\omega)$ in the asymmetric range, $\omega_{\rm FL}^- < \omega < \omega_{\rm FL}^+$, with $\omega_{\rm FL}^+ \approx \frac{1}{3}\omega_{\rm FL}^-$ (indicated by vertical dash-dotted red lines) and for the orbital and spin susceptibilities in the symmetric range, $|\omega| < \omega_{\rm FL}^+$. The vertical solid yellow line at $\omega < 0$ denotes the energy scale $\omega_{\rm cr}^-$ of the maximum in $\mathrm{Re}\,\Sigma(\omega)$ at $\omega < 0$. In (b), $\omega_{\rm cr}^+ = -\frac{1}{3}\omega_{\rm cr}^-$ marks the kink in $\mathrm{Re}\,\Sigma(\omega)$ at $\omega > 0$. Filled dots and open squares mark the orbital and spin Kondo scales, respectively. The grey area in (a) indicates a systematic error in $\mathrm{Im}\,\Sigma(\omega)$ (cf. Sec. 3.2 of Ref. [73] for details).

but can occur on very different energy scales (depending on the value of Δ_b).

Asymmetry in the FL regime. The left panels of Fig. 13 zoom into the frequency regime below $T_{\rm spin}$ (marked by open squares in the right panels). Similar to the results of Ref. [76] we observe in Figs. 13(a), 13(c), and 13(e) that FL behavior holds up to different frequency scales, $\omega_{\rm FL}^-$ and $\omega_{\rm FL}^+$, at $\omega < 0$ and $\omega > 0$ (cf. vertical red dash-dotted lines), respectively. These FL scales have been identified in $A(\epsilon_k, \omega)$ in the main text. The FL behavior is indicated by the red dashed curves in Figs. 13(a), 13(c), and 13(e): a parabola for $-\mathrm{Im}\,\Sigma(\omega)$ in panel (a), a linear fit for $\mathrm{Re}\,\Sigma(\omega)$ in panel (c), and a parabola for $A(\omega)$ in panel (e). Clearly, the black DMFT+NRG results deviate earlier from the red FL curves on the positive frequency side, i.e., at a lower scale $\omega_{\rm FL}^+ \approx \frac{1}{3}\omega_{\rm FL}^-$. Furthermore, we find that the position of the maximum of $A(\omega)$ approximately coincides with $\omega_{\rm FL}^+$.

In Figs. 13(g) and 13(i) we show the imaginary and the real parts of the dynamical orbital and spin susceptibilities, $\chi_{\rm orb}(\omega)$ and $\chi_{\rm spin}(\omega)$ [cf. Eq. (5)], respectively. The imaginary part of the dynamical susceptibility is defined as $\chi''(\omega) \equiv -\frac{1}{\pi}\mathrm{Im}\,\chi(\omega)$, the real part as $\chi'(\omega) \equiv \mathrm{Re}\,\chi(\omega)$. In contrast to $\Sigma(\omega)$ and $A(\omega)$ these quantities are particle-hole symmetric. The imaginary parts of both the orbital and spin susceptibilities follow the red dashed linear FL fit only for $|\omega| \lesssim \omega_{\rm FL}^+$. Accordingly, the real part of the spin susceptibility $\chi'_{\rm spin}(\omega)$ also exhibits parabolic FL scaling in this regime, while the real part of the orbital susceptibility $\chi'_{\rm orb}(\omega)$ is essentially constant.

In this paper we define the orbital and spin Kondo scales, $T_{\rm orb}$ and $T_{\rm spin}$ (cf. open squares and filled circles in Fig. 13), below which Kondo screening of the local orbital or spin degrees of freedom sets in, as the peak positions of $\chi''_{\rm orb}(\omega)$ and $\chi''_{\rm spin}(\omega)$, respectively. As usual for crossover scales, other definitions are possible, which would differ from ours by constant prefactors.

Appendix B: On the definition of crossover scales

Unlike a phase transition occurring at a well-defined critical temperature, spin screening is a crossover phenomenon, which cannot be described in terms of just a single number. This was understood very early in the classic work of K. Wilson [110]. To set the stage for the discussion of the Hund-Mott problem discussed in the main text, we here summarize some of Wilson's results for the temperature dependence of the impurity contribution to the spin susceptibility $\chi_{\rm imp}(T)$. (For a detailed discussion, see Section IX of Ref. [110] or Section 4.6 in Hewson's book [111].)

Wilson studied the single-impurity Kondo model, involving a single spin-$\frac{1}{2}$ impurity coupled to a conduction band with a featureless (flat) density of state. He considered the weak-coupling limit, where the impurity-bath exchange coupling $J_{\rm K}$ is much smaller than the bandwidth W. He showed that in this limit the temperature dependence of physical quantities can be described in terms of a crossover scale, the Kondo temperature $T_{\rm K}$, and a universal scaling function, $F(T/T_{\rm K})$. For example $\chi_{\rm imp}(T)$ has the form [112–114]

$$\chi_{\rm imp}(T) = \frac{F(T/T_{\rm K})}{T}\,. \tag{B1}$$

The meaning of Eq. (B1) is that as long as the temperature is much smaller than the bandwidth, $T \ll W$, the dependence of $\chi_{\rm imp}(T)$ on the model parameters $J_{\rm K}$ and W enters only via the scale $T_{\rm K}$. Still, this does not mean that spin screening "occurs at $T_{\rm K}$", as is sometimes asserted in the literature. Both the scale $T_{\rm K}$ *and* the scaling function F are needed to characterize the full crossover from an unstable high-temperature fixed point to a stable low-temperature fixed point.

Wilson computed the scaling function F numerically using his newly-developed numerical renormalization group approach. Fitting his numerical results, he found that $\chi_{\rm imp}(T)$ is well described by the following three functional forms, applicable for high, intermediate, and low temperatures, respectively (cf. Eq. (4.53) of Ref. [111]):

$$\chi_{\rm imp}(T) \simeq \begin{cases} \frac{1}{4T}\Big[1 - \frac{1}{\ln(T/T_{\rm K})} + \frac{\ln[\ln(T/T_{\rm K})]}{2[\ln(T/T_{\rm K})]^2} \\ \qquad + \mathcal{O}\Big(\frac{1}{[\ln(T/T_{\rm K})]^3}\Big)\Big], & (T > T_2), \quad \text{(B2a)} \\ \frac{0.68}{4}\,\frac{1}{T+\sqrt{2}T_{\rm K}}, & (T_1 < T < T_2), \quad \text{(B2b)} \\ \frac{0.4132}{4T_{\rm K}}\Big[1 - \mathcal{O}\left(\frac{T}{T_{\rm K}}\right)^2\Big], & (T < T_1). \quad \text{(B2c)} \end{cases}$$

Several comments are in order. First, Wilson defined $T_{\rm K}$ via a high-temperature condition, namely that the expansion (B2a) of $T\chi_{\rm imp}(T)$ should not contain a $[\ln(T/T_{\rm K})]^{-2}$ term. Notice, however, that the definition of $T_{\rm K}$ in terms of bare parameters is not unique, as it depends on the cutoff procedure, as discussed by Wilson himself or in Hewson's book [111]. Indeed, a change in the definition of $T_{\rm K}$ can always be compensated by a change in the scaling function F.

Second, T_2 and T_1 are the scales where deviations from the high- or low-temperature forms, (B2a) or (B2c), first become noticeable when T is decreased below T_2 or increased above T_1, respectively. Their values depend on the definition of $T_{\rm K}$; for that of Wilson, they are given by $T_2 = 16T_{\rm K}$ and $T_1 = 0.5T_{\rm K}$ (see Eq. (IX.99) in Ref. [110] and Hewson [111]). In the parlance of the main text of this paper, they may be viewed as the onset and completion of spin screening scales, $T_{\rm spin}^{\rm onset}$ and $T_{\rm spin}^{\rm cmp}$, respectively.

Third, we discuss the three functional forms given above. The high-temperature fixed point describes an essentially free local moment. Correspondingly, the high-temperature susceptibility, Eq. (B2a), shows Curie behavior $\chi_{\rm imp} \sim 1/T$ with logarithmic corrections due to

a marginally relevant operator. The crossover regime of intermediate temperatures shows Curie-Weiss behavior, Eq. (B2b). The overall prefactor, 0.68/4, is about 30% smaller than the prefactor 1/4 of the pure Curie law (B2a), reflecting the renormalization of the impurity magnetization due to the onset of screening with lowering temperature. The low-temperature fixed point describes FL excitations scattering off a fully screened impurity. Correspondingly, the low-temperature susceptibility, Eq. (B2c), approaches a constant for $T/T_{\rm K} \to 0$, with a $(T/T_{\rm K})^2$ correction caused by a leading irrelevant operator. The zero-temperature value of $4T_{\rm K}\chi_{\rm imp}(0) = 0.4132$, known as the Wilson number, is a characteristic property of the crossover function, linking properties of the high-and low-temperature fixed points.

Fourth, we note that an exact expression for the scaling function F was later obtained using the Bethe Ansatz, [115–117]. In particular, Andrei and Lowenstein obtained an analytical expression for the Wilson number [115]. The definitions of $T_{\rm K}$ used in the Bethe Ansatz papers differ from that of Wilson, but the universal behavior of the susceptibility agrees with Wilson's solution. The universality results from two facts: first, the impurity model is studied at very weak coupling ($J_{\rm K} \ll W$), and second, there is only one (marginally) relevant operator perturbing the unstable fixed point [111].

Fifth, we note for completeness that Wilson's version of our Eq. (B2b), namely his (IX.99), contains a factor 2 instead of $\sqrt{2}$ in the denominator. That is a typo, first noticed by Mel'nikov [118], see p. 503 of Ref. [117], and also Ref. [111], below Eq. (4.60).

To conclude our summary of Wilson's results on $\chi_{\rm imp}(T)$, we emphasize again that spin screening is a gradual crossover phenomenon, even in the simple context of the Kondo impurity model. To describe the crossover quantitatively, it does not suffice to specify just a single number for the crossover scale, even when only a single scale is dynamically generated. Instead, one also has to specify which observable and which scaling function was used, and the precise criteria used to define the crossover scale.

Now let us discuss the relevance of the above arguments for the present paper. DMFT maps the Hund-Hubbard lattice model that we consider in the main text to a quantum impurity model with a self-consistent bath. The bath is described by a hybridization function, which, in contrast to the pure Kondo model studied by Wilson, has a non-trivial structure. Moreover, this structure depends on temperature. Nevertheless Wilson's NRG approach for solving impurity models has been generalized to accommodate these complications, and indeed is now a widely-used impurity solver for DMFT.

Some of the terminology introduced by Wilson and reviewed above can also be used to understand some aspects of the solution of the DMFT equations and to illuminate the physics of the problem. For Hund metals, we have shown in Ref. [33] that an impurity with a rigid (not self-consistent) bath is a good guide to the full DMFT solution. Moreover, we argued there that Hund metals can be characterized by the criterion that the crossover scales for spin and orbital screening differ strongly, $T_{\rm spin} \ll T_{\rm orb}$, implying SOS, to identify a Hund metal. In that work, as here, we defined $T_{\rm spin}$ and $T_{\rm orb}$ as the energy scales at which the imaginary parts of the zero-temperature dynamical spin and orbital susceptibilities are maximal. We emphasize, though, that the occurrence or not of spin-orbital separation does not depend on the criteria used to define these crossover scales. For example, the onset-of-screening scales discussed in Sec. V A likewise yield $T_{\rm spin}^{\rm onset} \ll T_{\rm orb}^{\rm onset}$ for the Hund system H1.

In Ref. [7], we refined our discussion of crossover scales by analyzing the temperature dependence of the spin and orbital susceptibilities, $\chi_{\rm spin}(T)$ and $\chi_{\rm orb}(T)$. We introduced onset-of-screening scales $T_{\rm spin}^{\rm onset}$, $T_{\rm orb}^{\rm onset}$ below which deviations (say by x_1%) from pure Curie behavior set in, and completion-of-screening scales $T_{\rm spin}^{\rm cmp}$, $T_{\rm orb}^{\rm cmp}$ above which deviations (say by x_2%) from pure Pauli behavior set in. They correspond to Wilson's T_2 and T_1 scales, respectively. These operational definitions have some degree of arbitrariness (through the choices of x_1 and x_2; in fact, these were not even specified in Ref. [7]). However, they have the advantage that they can also be applied when the crossover function in the intermediate temperature regime does not have a simple analytical form, a situation generally encountered for self-consistent DMFT impurity models. We argued in Ref. [7] that the onset temperatures are useful to distinguish Mott systems from Hund systems: in Hund systems we have $T_{\rm spin}^{\rm onset} \ll T_{\rm orb}^{\rm onset}$, but in Mott systems $T_{\rm spin}^{\rm onset} \simeq T_{\rm orb}^{\rm onset}$, since the onset of spin and orbital screening with decreasing temperature occurs around the same temperature $T_{\rm M}$ at which a quasiparticle peak begins to emerge from the Mott pseudogap. Again, this distinction between Hund and Mott systems does not depend on the precise criteria used to define the onset scales.

In the main text of the present paper, we refined our discussion of crossover scales somewhat more. We exploited the freedom in the choice of definition of the onset and completion scales (i.e., of x_2 and x_1) to reduce the number of parameters by defining $T_{\rm orb}^{\rm cmp} \simeq T_{\rm spin}^{\rm onset}$ for Hund systems and $T_{\rm orb}^{\rm cmp} \simeq T_{\rm spin}^{\rm cmp}$ for Mott systems. These choices, compatible with our data for H1 and M1, have simple physical interpretations: For Hund systems, featuring SOS, spin screening sets in once orbital screening is complete. By contrast, for Mott systems, spin and orbital screening go hand in hand: just as both onset-of-screening scales coincide with the emergence of a quasiparticle peak from the Mott pseudogap and therefore match, $T_{\rm spin}^{\rm onset} \simeq T_{\rm orb}^{\rm onset} \simeq T_{\rm M}$, the completion-of-screening scales match, too, $T_{\rm orb}^{\rm cmp} \simeq T_{\rm spin}^{\rm cmp}$.

As a final remark, we note that one may attempt [42, 119, 120] to characterize the spin susceptibility $\chi_0(T)$ of Hund systems using the Curie-Weiss (CW) form $\chi_0^{\rm CW}(T) = \mu/(T+\theta)$, with θ serving as a crossover scale. The CW form applies if a plot of $1/\chi_0(T)$ vs T yields a

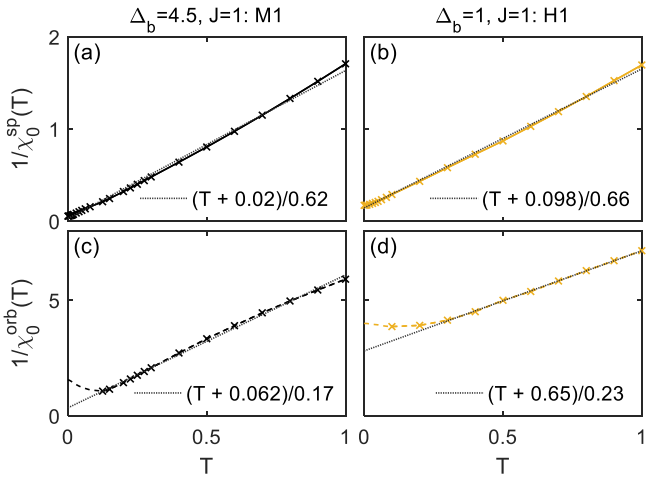

FIG. 14. Testing the applicability of a Curie-Weiss (CW) form for various susceptibilities by replotting the data from Fig. 7(c) as $1/\chi_0(T)$ vs T. The top row shows the spin susceptibilities of M1 (left) and H1 (right) using solid lines, the bottom row the same for the orbital susceptibilities, using dashed lines. Dotted lines show Curie-Weiss fits to those data points (shown using crosses) for temperatures higher than the temperature at which $\chi_0(T)$ is maximal.

straight line. Figures 14(a) and 14(b) show such plots for the spin susceptibilities of M1 and H1. The resulting curves show clear deviations from linear behavior, in particular for large T. Therefore, CW fits (dotted lines) characterize these susceptibilities only fairly crudely (see also Refs. [119, 120]). For completeness, Figs. 14(c) and 14(d) show analogous plots of the orbital susceptibilities. These curves are strongly nonlinear in the low-temperature regime corresponding to the completion of orbital screening, where the CW form is not applicable at all.

Appendix C: Temperature dependence of optical conductivity

We next study the optical conductivity $\sigma(\omega)$ [cf. Eq. (D1)] again for system I2. $\sigma(\omega)$ is plotted on a linear and a logarithmic frequency scale in Figs. 15(a) and 15(b), respectively. For comparison, we also show data for W0 ($\Delta_b = 3.5$, $J = 0$), computed at $T = 0.15$, which is still in the FL temperature regime. At $T = 0$ we expect a FL Drude peak for I2. However, the data (cf. blue curve) is not accurate enough to resolve the FL behavior at very low frequencies, $\omega < \omega_{\rm FL}^{+}$ (cf. discussion of blue and red curves in Fig. 3.1(b) in Sec. 3.2 of Ref. [73]). In the low-frequency NFL crossover regime, here approximately given by $\omega_{\rm FL}^{+} \lesssim \omega \lesssim |\omega_{\rm cr}^{-}|$, we observe a power-law flank in $\sigma(\omega) \propto \omega^{-\alpha}$, with $\alpha \approx 7/5$ at $T = 0$. Notably, for $\omega > |\omega_{\rm cr}^{-}|$ a broad HQP shoulder develops around $T_{\rm orb}$ at $T = 0$.

With increasing temperature but below $T \lesssim T_{\rm spin}^{\rm onset} = 0.1$, spin degrees of freedom are gradually unscreened in the system while the orbitals are still screened. This process is reflected in $\sigma(\omega)$: with increasing temperature spectral weight is shifted from low frequencies into the HQP shoulder, while the high-frequency flank of $\sigma(\omega)$ remains unaffected. Note that the HQP shoulder is absent for $J = 0$ [cf. black curve in Figs. 15(a) and 15(b)]. At higher temperatures ($T > T_{\rm spin}^{\rm onset}$) the HQP shoulder gradually decreases in height, reflecting the unscreening of the orbital degrees of freedom in I2. The second shoulder at bare energy scales is a Hubbard-band feature, which is also present for $J = 0$. We suspect that the HQP shoulder at $\omega > |\omega_{\rm cr}^{-}|$ is an optical fingerprint of the HQP band [SU(3) Kondo resonance in $A(\omega)$] and can indeed be interpreted as Hund's-coupling-induced excess spectral weight, caused by resilient QPs, as suggested in Ref. [77]. Further, we remark that our results (for $T \lesssim T_{\rm spin}^{\rm onset}$) are reminiscent of recent optical conductivity measurements [68] for KFe_2As_2.

In Figs. 15(c) and 15(d) the kinetic energy $K(\Omega)$ [as defined in Eq. (D3)] is plotted as a function of frequency Ω for various temperatures. In Ref. [107] an unusual spectral weight transfer from low to high energies was observed at low temperatures in $K(\Omega)$ for iron pnictides. This observation would correspond to line crossings of different $K(\Omega, T)$ curves for $J = 2$ in Figs. 15(c) and 15(d), which is yet not found in our data. We remark that this might be due to the rather large $\Delta_b = 3.5$.

Appendix D: Elementary definitions and relations

1. Optical conductivity, kinetic energy, resistivity, and the Mott-Ioffe-Regel (MIR) limit

Optical conductivity. The (real part of the) optical conductivity (per spinful band), computed in linear response, is given by Ref. [76],

$$\sigma(\omega) = \frac{2\pi e^2}{\hbar} \int \mathrm{d}\omega' \, \frac{f(\omega') - f(\omega+\omega')}{\omega} \times \int \mathrm{d}\varepsilon \, \Phi(\varepsilon) A(\varepsilon,\omega') A(\varepsilon,\omega+\omega'), \tag{D1}$$

where $f(\omega)$ is the Fermi function, $A(\varepsilon,\omega)$ the structure factor as defined in Eq. (4), and $\Phi(\varepsilon)$ the transport velocity kernel,

$$\Phi(\varepsilon) = \int \frac{\mathrm{d}^d k}{(2\pi)^d} \left(\frac{\partial \varepsilon_{\mathbf{k}}}{\partial k_x}\right)^2 \delta(\varepsilon - \varepsilon_{\mathbf{k}}) \tag{D2a}$$

$$= \Phi(0) \left[1 - \left(\frac{\varepsilon}{D}\right)^2\right]^{\frac{3}{2}}. \tag{D2b}$$

The latter is here expressed through the band velocity in x direction, $v_{\mathbf{k}}^x = \frac{\partial \varepsilon_{\mathbf{k}}}{\hbar \partial k_x}$, and Eq. (D2b) follows for the Bethe lattice.

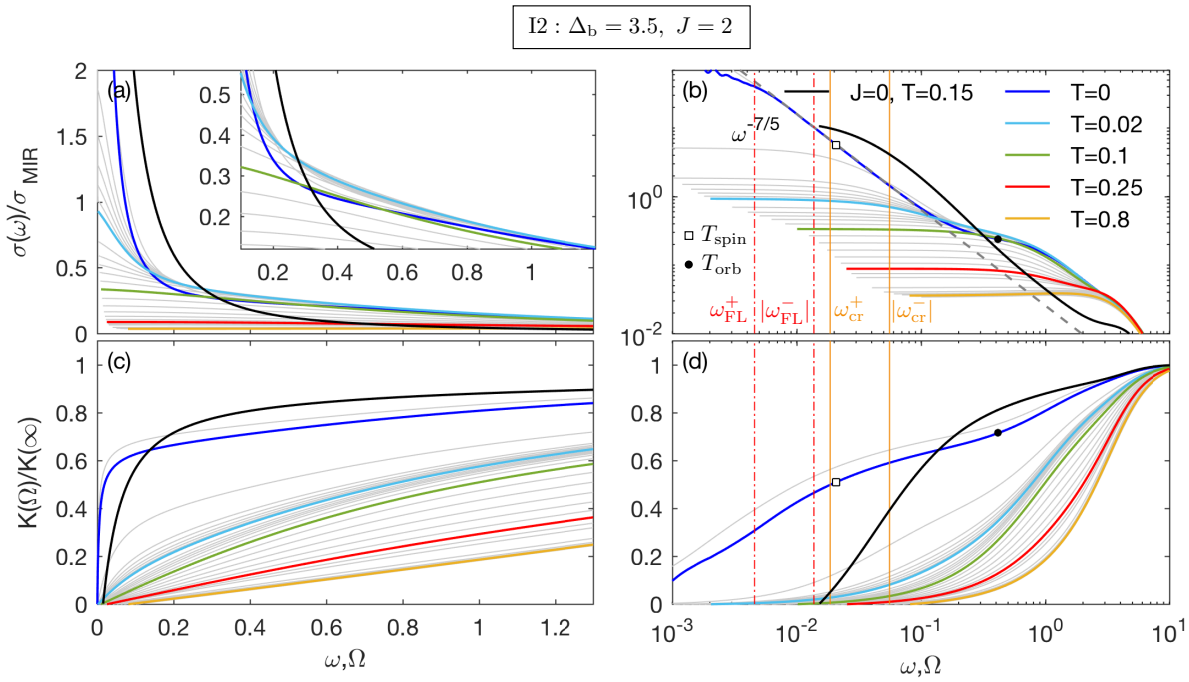

FIG. 15. [(a),(b)] The optical conductivity $\sigma(\omega)$ and the kinetic energy $K(\Omega)$ are plotted for various temperatures on [(a),(c)] a linear and [(b),(d)] a logarithmic frequency scale for I2 ($\Delta_b = 3.5$, $J = 2$). In addition, data for W0 ($\Delta_b = 3.5$, $J = 0$) at $T = 0.15$ is shown in black. [(b),(d)] $|\omega^{\pm}_{\rm FL}|$, below which FL behavior should set in, is marked by vertical dash-dotted red lines. The vertical solid yellow lines denote $|\omega^{\pm}_{\rm cr}|$. Filled dots and open squares mark the orbital and spin Kondo scales, respectively.

Kinetic energy. The kinetic energy $K(\Omega)$ is the integral of the optical conductivity $\sigma(\omega)$ up to a cutoff value Ω [107]:

$$\frac{K(\Omega)}{K(\infty)} = \frac{\int_0^{\Omega} {\rm d}\omega\, \sigma(\omega)}{\int_0^{\infty} {\rm d}\omega\, \sigma(\omega)}. \tag{D3}$$

We normalize $K(\Omega)$ to $K(\infty)$.

Resistivity. The temperature-dependent optical resistivity is given as the inverse of the optical conductivity evaluated at the Fermi level, $\omega = 0$,

$$\rho(T) = \frac{1}{\sigma(\omega = 0, T)}. \tag{D4}$$

Mott-Ioffe-Regel (MIR) limit. In conventional metals $\rho(T)$ increases with temperature. This behavior can be explained in a QP picture: the mean-free path l of a QP gradually decreases because thermally-induced scattering events become more frequent. For phonon scattering at higher temperatures, i.e., above a small temperature below which electron-electron scattering is dominant, this leads to a linear growth of $\rho(T) \sim T$. However, this QP picture breaks down approximately when l becomes shorter than the interatomic spacing, leading to the Mott-Ioffe-Regel (MIR) limit, $k_{\rm F} l_{\rm min} \approx 2\pi$ [121–123] (another popular definition is $k_{\rm F} l_{\rm min} \approx 1$). As a consequence, above a corresponding MIR temperature $T_{\rm MIR}$, the resistivity saturates in conventional metals, approaching a maximum value $\rho_{\rm MIR}$. While for most good metals, $l \gg 2\pi/k_{\rm F}$ holds up to their melting temperatures, there is a vast number of metals for which the MIR resistivity saturation is observed [124]. Interestingly, most strongly correlated metals, like cuprate high-temperature superconductors (HTSCs), heavy fermions, Hund metals (including iron-based HTSCs), and also several organic compounds exceed the MIR limit and $\rho(T)$ does *not* saturate with increasing temperature. Due to this unconventional but common feature, which is generically assumed to be induced by some kind of NFL behavior, all these materials are collectively referred to as "bad metals" in the literature [124, 125].

In Fig. 15 $\sigma(\omega)$ is measured in units of $\sigma_{\rm MIR} = \frac{2\pi e^2 \Phi(0)}{\hbar D}$. This is the MIR limit derived in Ref. [76] for a free parabolic band in two dimensions, $\varepsilon(\mathbf{k}) = \frac{\hbar^2(k_x^2+k_y^2)}{2m}$, using the criterion $k_{\rm FL} l_{\rm min} = 2\pi$. Accordingly, in Fig. 9 we plot ρ in units of $\rho_{\rm MIR} = 1/\sigma_{\rm MIR}$.

2. Thermopower

The thermopower (Seebeck coefficient) is defined as $\alpha(T) = -\Delta\mathcal{V}/\Delta T$, where $-\Delta\mathcal{V}$ is the electric field generated when a thermal gradient ΔT is established in a material under conditions which are such that no electrical current flows [42]. We calculate $\alpha(T)$ with the Kubo

formula of Ref. [42],

$$\alpha(T) = -\frac{k_B}{e}\frac{\int \mathrm{d}\omega\, T(\omega)\beta\omega\left(-\frac{\partial f}{\partial\omega}\right)}{\int \mathrm{d}\omega\, T(\omega)\left(-\frac{\partial f}{\partial\omega}\right)}, \tag{D5}$$

where $\beta = 1/k_\mathrm{B}T$, and the transport function $T(\omega)$ given here for transport in x direction, reads

$$\begin{aligned} T(\omega) &= 2\pi e^2 \int \frac{\mathrm{d}^d k}{(2\pi)^d}\, (v_\mathbf{k}^x)^2\, A_\mathbf{k}(\omega)^2 \\ &= \frac{2\pi e^2}{\hbar^2}\int \mathrm{d}\varepsilon\, \Phi(\varepsilon) A(\varepsilon,\omega)^2. \end{aligned} \tag{D6}$$

3. Entropy

Within DMFT, where a lattice system is mapped self-consistently onto an impurity system, we can both calculate the impurity contribution to the entropy, as usually done within NRG [126], and the lattice entropy. Importantly, these entropies differ (quantitatively but not qualitatively), as is discussed in detail in Sec. VI F.

Impurity contribution. The impurity contribution to the entropy S_imp is introduced in Eqs. (48) and (53) of Ref. [126] as the difference,

$$S_\mathrm{imp}(T) = S_\mathrm{tot}(T) - S_\mathrm{tot}^{(0)}(T), \tag{D7}$$

between the entropy of the total Wilson chain S_tot and the entropy of a reference system $S_\mathrm{tot}^{(0)}$, which is the bare conduction Hamiltonian without impurity. In practice, it is thus necessary to perform two independent NRG runs, one for the full Hamiltonian and one for the same Hamiltonian without impurity.

Lattice entropy. Starting from the thermodynamic relation $T(\partial S_\mathrm{latt}/\partial T) = \partial \mathcal{E}_\mathrm{latt}/\partial T$ between the entropy and the total internal energy of the lattice, the lattice entropy can be expressed as an integral involving the specific heat, $C(T) = (\partial \mathcal{E}_\mathrm{latt}/\partial T)$,

$$S_\mathrm{latt}(T) = S_\mathrm{latt}(T_0) + \int_{T_0}^{T} \mathrm{d}T'\, \frac{C(T')}{T'}\,, \tag{D8}$$

following Eq. (238) of Ref. [4]. $S_\mathrm{latt}(T_0)$ is a constant offset, in principle unknown. In the case of a FL, however, $S_\mathrm{latt}(T_0)$ can be determined exactly [cf. Eq. (7)]. For Hubbard-type models in the limit of large lattice coordination, the total internal energy is given by Eq. (7) of Ref. [127], which we apply in the form,

$$\begin{aligned} \frac{\mathcal{E}_\mathrm{latt}}{N_c} &= \int \mathrm{d}\omega\, f(\omega)(\omega+\mu)A(\omega) && \text{(D9a)} \\ &\quad + 2t^2 \int \mathrm{d}\omega_1 \int \mathrm{d}\omega_2\, f(\omega_1)\frac{A(\omega_1)A(\omega_2)}{\omega_1-\omega_2} \\ &= \int \mathrm{d}\omega\, f(\omega)(\omega+\mu)A(\omega) && \text{(D9b)} \\ &\quad - \frac{2t^2}{\pi}\int \mathrm{d}\omega\, f(\omega)\mathrm{Re}\,G(\omega)\mathrm{Im}\,G(\omega). \end{aligned}$$

Here $f(\omega)$ is the Fermi function, and the second equality follows via the Kramers-Kronig relation, $\mathrm{Re}\,G(\omega) = \frac{1}{\pi}P\int \mathrm{d}\omega' \frac{\mathrm{Im}\,G(\omega')}{\omega'-\omega} = P\int \mathrm{d}\omega' \frac{A(\omega')}{\omega-\omega'}$.

[1] D. B. McWhan, T. M. Rice, and J. P. Remeika, Phys. Rev. Lett. **23**, 1384 (1969).
[2] D. B. McWhan, J. P. Remeika, J. P. Maita, H. Okinaka, K. Kosuge, and S. Kachi, Phys. Rev. B **7**, 326 (1973).
[3] D. B. McWhan, A. Menth, J. P. Remeika, W. F. Brinkman, and T. M. Rice, Phys. Rev. B **7**, 1920 (1973).
[4] A. Georges, G. Kotliar, W. Krauth, and M. J. Rozenberg, Rev. Mod. Phys. **68**, 13 (1996).
[5] P. A. Lee, N. Nagaosa, and X.-G. Wen, Rev. Mod. Phys. **78**, 17 (2006).
[6] X. Deng, A. Sternbach, K. Haule, D. N. Basov, and G. Kotliar, Phys. Rev. Lett. **113**, 246404 (2014).
[7] X. Deng, K. M. Stadler, K. Haule, A. Weichselbaum, J. von Delft, and G. Kotliar, Nat. Commun. **10**, 2721 (2019).
[8] P. Werner, E. Gull, M. Troyer, and A. J. Millis, Phys. Rev. Lett **101**, 166405 (2008).
[9] K. Haule and G. Kotliar, New J. Phys. **11**, 025021 (2009).
[10] Z. P. Yin, K. Haule, and G. Kotliar, Nat. Phys. **7**, 294 (2011).
[11] Z. P. Yin, K. Haule, and G. Kotliar, Nat. Mater. **10**, 932 (2011).
[12] N. Lanatà, H. U. R. Strand, G. Giovannetti, B. Hellsing, L. de' Medici, and M. Capone, Phys. Rev. B **87**, 045122 (2013).
[13] L. Fanfarillo, G. Giovannetti, M. Capone, and E. Bascones, Phys. Rev. B **95**, 144511 (2017).
[14] A. Kostin, P. O. Sprau, A. Kreisel, Y. X. Chong, A. E. Böhmer, P. C. Canfield, P. J. Hirschfeld, B. M. Andersen, and J. C. S. Davis, Nat. Mater. **17**, 869 (2018).
[15] L. Huang and H. Lu, Phys. Rev. B **102**, 125130 (2020).
[16] C.-Y. Moon, npj Comput. Mater. **6**, 147 (2020).
[17] C. Watzenböck, M. Edelmann, D. Springer, G. Sangiovanni, and A. Toschi, Phys. Rev. Lett. **125**, 086402 (2020).
[18] T. Gorni, P. Villar Arribi, M. Casula, and L. de' Medici, Phys. Rev. B **104**, 014507 (2021).
[19] P. Villar Arribi and L. de' Medici, arXiv:2104.11018.
[20] L. de' Medici, J. Mravlje, and A. Georges, Phys. Rev. Lett. **107**, 256401 (2011).
[21] Z. P. Yin, K. Haule, and G. Kotliar, Phys. Rev. B **86**, 195141 (2012).
[22] J. Mravlje, M. Aichhorn, T. Miyake, K. Haule, G. Kotliar, and A. Georges, Phys. Rev. Lett. **106**, 096401 (2011).

[23] H. T. Dang, J. Mravlje, A. Georges, and A. J. Millis, Phys. Rev. B **91**, 195149 (2015).
[24] F. B. Kugler, M. Zingl, H. U. R. Strand, S.-S. B. Lee, J. von Delft, and A. Georges, Phys. Rev. Lett. **124**, 016401 (2020).
[25] M. Zingl, J. Mravlje, M. Aichhorn, O. Parcollet, and A. Georges, npj Quantum Mater. **4** (2019).
[26] N.-O. Linden, M. Zingl, C. Hubig, O. Parcollet, and U. Schollwöck, Phys. Rev. B **101**, 041101 (2020).
[27] N. Dasari, S. R. K. C. S. Yamijala, M. Jain, T. S. Dasgupta, J. Moreno, M. Jarrell, and N. S. Vidhyadhiraja, Phys. Rev. B **94**, 085143 (2016).
[28] H. J. Lee, C. H. Kim, and A. Go, Phys. Rev. B **102**, 195115 (2020).
[29] J. Clepkens, A. W. Lindquist, and H.-Y. Kee, Phys. Rev. Research **3**, 013001 (2021).
[30] A. Georges, L. de' Medici, and J. Mravlje, Annu. Rev. Condens. Matter Phys. **4**, 137 (2013).
[31] E. Bascones, B. Valenzuela, and M. J. Calderón, C. R. Phys. **17**, 36 (2016).
[32] L. de' Medici, Autumn School on Correlated Electrons, Jülich (Germany), 25–29.09.2017 (Forschungszentrum Jülich GmbH Zentralbibliothek, Verlag, Jülich, 2017) Chap. 14, pp. 14.2–14.22.
[33] K. M. Stadler, Z. P. Yin, J. von Delft, G. Kotliar, and A. Weichselbaum, Phys. Rev. Lett. **115**, 136401 (2015).
[34] C. Aron and G. Kotliar, Phys. Rev. B **91**, 041110 (2015).
[35] K. M. Stadler, G. Kotliar, A. Weichselbaum, and J. von Delft, Ann. Phys. **405**, 365 (2018).
[36] F. B. Kugler, S.-S. B. Lee, A. Weichselbaum, G. Kotliar, and J. von Delft, Phys. Rev. B **100**, 115159 (2019).
[37] Y. Wang, E. Walter, S.-S. B. Lee, K. M. Stadler, J. von Delft, A. Weichselbaum, and G. Kotliar, Phys. Rev. Lett. **124**, 136406 (2020).
[38] A. Horvat, R. Žitko, and J. Mravlje, arXiv:1907.07100.
[39] E. Walter, K. M. Stadler, S.-S. B. Lee, Y. Wang, G. Kotliar, A. Weichselbaum, and J. von Delft, Phys. Rev. X **10**, 031052 (2020).
[40] J. Karp, M. Bramberger, M. Grundner, U. Schollwöck, A. J. Millis, and M. Zingl, Phys. Rev. Lett. **125**, 166401 (2020).
[41] S. Hoshino and P. Werner, Phys. Rev. Lett. **115**, 247001 (2015).
[42] J. Mravlje and A. Georges, Phys. Rev. Lett. **117**, 036401 (2016).
[43] Y. Wang, C.-J. Kang, H. Miao, and G. Kotliar, Phys. Rev. B **102**, 161118 (2020).
[44] B. Kang, C. Melnick, P. Semon, S. Ryee, M. J. Han, G. Kotliar, and S. Choi, (2020), arXiv:2007.14610.
[45] J. Rincón, A. Moreo, G. Alvarez, and E. Dagotto, Phys. Rev. B **90**, 241105 (2014).
[46] A. S. Belozerov, A. A. Katanin, and V. I. Anisimov, Phys. Rev. B **97**, 115141 (2018).
[47] A. Mezio and R. H. McKenzie, Phys. Rev. B **100**, 205134 (2019).
[48] J. I. Facio and P. S. Cornaglia, J. Phys.: Condens. Matter **31**, 245602 (2019).
[49] J. Steinbauer, L. de' Medici, and S. Biermann, Phys. Rev. B **100**, 085104 (2019).
[50] S. Y. Song, J. H. J. Martiny, A. Kreisel, B. M. Andersen, and J. Seo, Phys. Rev. Lett. **124**, 117001 (2020).
[51] P. Coleman, Y. Komijani, and E. J. König, Phys. Rev. Lett. **125**, 077001 (2020).
[52] M. Chatzieleftheriou, M. Berović, P. Villar Arribi, M. Capone, and L. de' Medici, Phys. Rev. B **102**, 205127 (2020).
[53] H. J. Lee, C. H. Kim, and A. Go, arXiv:2107.05906.
[54] D. van der Marel and G. A. Sawatzky, Phys. Rev. B **37**, 10674 (1988).
[55] A. A. Khajetoorians, M. Valentyuk, M. Steinbrecher, T. Schlenk, A. Shick, J. Kolorenc, A. I. Lichtenstein, T. O. Wehling, R. Wiesendanger, and J. Wiebe, Nat. Nanotechnol. **10**, 958 (2015).
[56] X. Chen, I. Krivenko, M. B. Stone, A. I. Kolesnikov, T. Wolf, D. Reznik, K. S. Bedell, F. Lechermann, and S. D. Wilson, Nat. Commun. **11**, 3076 (2020).
[57] B. G. Jang, G. Han, I. Park, D. Kim, Y. Y. Koh, Y. Kim, W. Kyung, H.-D. Kim, C.-M. Cheng, K.-D. Tsuei, K. D. Lee, N. Hur, J. H. Shim, C. Kim, and G. Kotliar, Nat. Commun. **12**, 1208 (2021).
[58] A. Richaud, M. Ferraretto, and M. Capone, Phys. Rev. B **103**, 205132 (2021).
[59] L. de' Medici, Phys. Rev. B **83**, 205112 (2011).
[60] L. de' Medici, S. R. Hassan, M. Capone, and X. Dai, Phys. Rev. Lett. **102**, 126401 (2009).
[61] L. de' Medici, G. Giovannetti, and M. Capone, Phys. Rev. Lett. **112**, 177001 (2014).
[62] L. Fanfarillo and E. Bascones, Phys. Rev. B **92**, 075136 (2015).
[63] F. Hund, Z. Phys. **33**, 345 (1925).
[64] I. Okada and K. Yosida, Prog. Theor. Phys. **49**, 1483 (1973).
[65] K. Haule, J. H. Shim, and G. Kotliar, Phys. Rev. Lett. **100**, 226402 (2008).
[66] F. Hardy, A. E. Böhmer, D. Aoki, P. Burger, T. Wolf, P. Schweiss, R. Heid, P. Adelmann, Y. X. Yao, G. Kotliar, J. Schmalian, and C. Meingast, Phys. Rev. Lett. **111**, 027002 (2013).
[67] F. Hardy, A. E. Böhmer, L. de' Medici, M. Capone, G. Giovannetti, R. Eder, L. Wang, M. He, T. Wolf, P. Schweiss, R. Heid, A. Herbig, P. Adelmann, R. A. Fisher, and C. Meingast, Phys. Rev. B **94**, 205113 (2016).
[68] R. Yang, Z. Yin, Y. Wang, Y. Dai, H. Miao, B. Xu, X. Qiu, and C. C. Homes, Phys. Rev. B **96**, 201108 (2017).
[69] S. Ryee, M. J. Han, and S. Choi, Phys. Rev. Lett. **126**, 206401 (2021).
[70] A. Weichselbaum and J. von Delft, Phys. Rev. Lett. **99**, 076402 (2007).
[71] A. Weichselbaum, Ann. Phys. **327**, 2972 (2012).
[72] A. Weichselbaum, Phys. Rev. B **86**, 245124 (2012).
[73] K. M. Stadler, Ph.D. thesis, Ludwig Maximilian University of Munich (2019).
[74] T.-H. Lee, A. Chubukov, H. Miao, and G. Kotliar, Phys. Rev. Lett. **121**, 187003 (2018).
[75] Y.-M. Wu, A. Abanov, and A. V. Chubukov, Phys. Rev. B **99**, 014502 (2019).
[76] X. Deng, J. Mravlje, R. Žitko, M. Ferrero, G. Kotliar, and A. Georges, Phys. Rev. Lett. **110**, 086401 (2013).
[77] D. Stricker, J. Mravlje, C. Berthod, R. Fittipaldi, A. Vecchione, A. Georges, and D. van der Marel, Phys. Rev. Lett. **113**, 087404 (2014).
[78] A. Tamai, M. Zingl, E. Rozbicki, E. Cappelli, S. Riccò, A. de la Torre, S. McKeown Walker, F. Y. Bruno, P. D. C. King, W. Meevasana, M. Shi, M. Radović, N. C. Plumb, A. S. Gibbs, A. P. Mackenzie, C. Berthod,

H. U. R. Strand, M. Kim, A. Georges, and F. Baumberger, Phys. Rev. X **9**, 021048 (2019).
[79] M. Hanl and A. Weichselbaum, Phys. Rev. B **89**, 075130 (2014).
[80] C. Yue and P. Werner, Phys. Rev. B **102**, 085102 (2020).
[81] A. Horvat, R. Žitko, and J. Mravlje, Phys. Rev. B **96**, 085122 (2017).
[82] M. Vojta, J. Low Temp. Phys. **161**, 203 (2010).
[83] L. de'Medici, A. Georges, and S. Biermann, Phys. Rev. B **72**, 205124 (2005).
[84] M. Ferrero, F. Becca, M. Fabrizio, and M. Capone, Phys. Rev. B **72**, 205126 (2005).
[85] M. Yi, D. H. Lu, R. Yu, S. C. Riggs, J.-H. Chu, B. Lv, Z. K. Liu, M. Lu, Y.-T. Cui, M. Hashimoto, S.-K. Mo, Z. Hussain, C. W. Chu, I. R. Fisher, Q. Si, and Z.-X. Shen, Phys. Rev. Lett. **110**, 067003 (2013).
[86] M. Bramberger, J. Mravlje, M. Grundner, U. Schollwöck, and M. Zingl, Phys. Rev. B **103**, 165133 (2021).
[87] A. J. Kim, H. O. Jeschke, P. Werner, and R. Valentí, Phys. Rev. Lett. **118**, 086401 (2017).
[88] D. Springer, B. Kim, P. Liu, S. Khmelevskyi, S. Adler, M. Capone, G. Sangiovanni, C. Franchini, and A. Toschi, Phys. Rev. Lett. **125**, 166402 (2020).
[89] S. Hoshino and P. Werner, Phys. Rev. B **93**, 155161 (2016).
[90] H. Alloul and A. Cano, C. R. Phys. **17**, 1 (2016).
[91] A. Isidori, M. Berović, L. Fanfarillo, L. de' Medici, M. Fabrizio, and M. Capone, Phys. Rev. Lett. **122**, 186401 (2019).
[92] P. Werner, S. Hoshino, and H. Shinaoka, Phys. Rev. B **94**, 245134 (2016).
[93] L. Fanfarillo, A. Valli, and M. Capone, Phys. Rev. Lett. **125**, 177001 (2020).
[94] T. Maier, M. Jarrell, T. Pruschke, and M. H. Hettler, Rev. Mod. Phys. **77**, 1027 (2005).
[95] G. Rohringer, H. Hafermann, A. Toschi, A. A. Katanin, A. E. Antipov, M. I. Katsnelson, A. I. Lichtenstein, A. N. Rubtsov, and K. Held, Rev. Mod. Phys. **90**, 025003 (2018).
[96] T. Ayral and O. Parcollet, Phys. Rev. B **92**, 115109 (2015).
[97] T. Ayral and O. Parcollet, Phys. Rev. B **93**, 235124 (2016).
[98] A. Toschi, A. A. Katanin, and K. Held, Phys. Rev. B **75**, 045118 (2007).
[99] K. Held, A. A. Katanin, and A. Toschi, Prog. Theor. Phys. Suppl. **176**, 117 (2008).
[100] A. N. Rubtsov, M. I. Katsnelson, and A. I. Lichtenstein, Phys. Rev. B **77**, 033101 (2008).
[101] S. Brener, H. Hafermann, A. N. Rubtsov, M. I. Katsnelson, and A. I. Lichtenstein, Phys. Rev. B **77**, 195105 (2008).
[102] C. Taranto, S. Andergassen, J. Bauer, K. Held, A. Katanin, W. Metzner, G. Rohringer, and A. Toschi, Phys. Rev. Lett. **112**, 196402 (2014).
[103] D. Vilardi, C. Taranto, and W. Metzner, Phys. Rev. B **97**, 235110 (2018).
[104] D. Vilardi, C. Taranto, and W. Metzner, Phys. Rev. B **99**, 104501 (2019).
[105] P. Sémon, K. Haule, and G. Kotliar, Phys. Rev. B **95**, 195115 (2017).
[106] S. Ryee, P. Sémon, M. J. Han, and S. Choi, npj Quantum Mater. **5**, 19 (2020).
[107] A. A. Schafgans, S. J. Moon, B. C. Pursley, A. D. LaForge, M. M. Qazilbash, A. S. Sefat, D. Mandrus, K. Haule, G. Kotliar, and D. N. Basov, Phys. Rev. Lett. **108**, 147002 (2012).
[108] H. Miao, L.-M. Wang, P. Richard, S.-F. Wu, J. Ma, T. Qian, L.-Y. Xing, X.-C. Wang, C.-Q. Jin, C.-P. Chou, Z. Wang, W. Ku, and H. Ding, Phys. Rev. B **89**, 220503 (2014).
[109] H. Miao, Z. P. Yin, S. F. Wu, J. M. Li, J. Ma, B.-Q. Lv, X. P. Wang, T. Qian, P. Richard, L.-Y. Xing, X.-C. Wang, C. Q. Jin, K. Haule, G. Kotliar, and H. Ding, Phys. Rev. B **94**, 201109 (2016).
[110] K. G. Wilson, Rev. Mod. Phys. **47**, 773 (1975).
[111] A. C. Hewson, *The Kondo problem to heavy fermions* (Cambridge University Press, 1993).
[112] G. Yuval and P. W. Anderson, Phys. Rev. B **1**, 1522 (1970).
[113] P. W. Anderson, G. Yuval, and D. R. Hamann, Phys. Rev. B **1**, 4464 (1970).
[114] P. Anderson, G. Yuval, and D. Hamann, Solid State Comm. **8**, 1033 (1970).
[115] N. Andrei and J. H. Lowenstein, Phys. Rev. Lett. **46**, 356 (1981).
[116] V. M. Filyov, A. M. Tsvelick, and P. B. Wiegmann, Phys. Lett. A **81**, 175 (1981).
[117] A. Tsvelick and P. Wiegmann, Adv. Phys. **32**, 453 (1983).
[118] V. I. Mel'nikov, JETP Lett. **35**, 511 (1982).
[119] A. A. Katanin, Nat. Commun. **12**, 1433 (2021).
[120] X. Deng, K. M. Stadler, K. Haule, S.-S. B. Lee, A. Weichselbaum, J. von Delft, and G. Kotliar, Nat. Commun. **12**, 1445 (2021).
[121] A. F. Ioffe and A. R. Regel, Prog. Semicond. **4**, 237 (1960).
[122] N. F. Mott, Phil. Mag. Series 8, **26**, 1015 (1972).
[123] M. Gurvitch, Phys. Rev. B **24**, 7404 (1981).
[124] N. E. Hussey, K. Takenaka, and H. Takagi, Phil. Mag. Series 8, **84**, 2847 (2004).
[125] V. J. Emery and S. A. Kivelson, Phys. Rev. Lett. **74**, 3253 (1995).
[126] R. Bulla, T. A. Costi, and T. Pruschke, Rev. Mod. Phys. **80**, 395 (2008).
[127] G. Kotliar, Eur. Phys. J. B **11**, 27 (1999).